remote sensing

MDPI

*Article*

# A Cost-Effective Approach to Estimate Quinoa Aboveground Biomass Volume Combining UAV RGB Data with Sentinel-1 and Sentinel-2 Satellite Imagery

**Diego Tola [1,2,3], Lautaro Bustillos [3,4], Fanny Arragan [4], Marco Patiño [4], Reinaldo Quispe [5], Tati Almeida [6], Henrique Roig [6], Raúl Espinoza-Villar [2], Ramiro Pillco Zolá [1] and Frédéric Satgé [1,3,*]**

[1] Instituto de Hidráulica e Hidrología (IHH), Universidad Mayor de San Andrés, La Paz 10077, Bolivia
[2] Programa de Doctorado en Recursos Hídricos (PDRH), Universidad Nacional Agraria La Molina, Lima 15024, Peru
[3] ESPACE-DEV, University Montpellier, IRD, University Antilles, University Guyane, University Réunion, 34093 Montpellier, France
[4] Facultad de Agronomía, Universidad Mayor de San Andrés, La Paz 10077, Bolivia
[5] Laboratorio de Entomología, Fundación PROINPA, La Paz 10077, Bolivia
[6] Graduate Program in Applied Geosciences and Geodynamics (PPGGAG), Institute of Geosciences (IG), University of Brasília (UnB), Brasília 70910-900, Brazil
* Correspondence: frederic.satge@ird.fr

## Highlights

**What are the main findings?**

- UAV-derived quinoa aboveground volume (ABV) estimates provide an effective alternative to sparse and poorly representative field-based measurements.
- Combined radar (Sentinel-1) and optical (Sentinel-2) observations improve ABV estimation through their complementary strengths.

**What are the implications of the main findings?**

- An easily scalable and transferable approach for monitoring ABV in remote agricultural regions.
- Promising prospects for inferring crop yield from ABV estimates to anticipate risks associated with low-yield production years.

## Abstract

This study assessed the integration of Unmanned Aerial Vehicles (UAVs) and satellite images (Sentinel-1 and Sentinel-2) in advanced machine-learning techniques to monitor the ABV of quinoa crops (Jacha Grano variety) across the Bolivian Altiplano. The proposed method follows a two-step procedure. First, UAV RGB images were used in photogrammetric and deep-learning (Convolutional Neural Networks-CNN) models to estimate reference quinoa ABVs at a 10 m spatial resolution from the crop canopy 3D model and classification, respectively. Secondly, several spectral and polarization/texture indices derived from Sentinel-2 and -1 images were integrated into three decision-tree-based machine-learning models (Random Forest-RF, Gradient Boosting-GB, eXtreme Gradient Boosting-XGB), and one CNN-based machine-learning model to estimate ABV. Additionally, a Stacking Model (STM) build on top of the three decision-tree-based models was considered for comparison. Model evaluation was also performed in a two-step approach. First, a 10-fold cross-validation strategy was used to highlight ABV sensitivity to Sentinel-2 and Sentinel-1 alone and in combination. Secondly, a Leave-One-Plot-Out Cross-Validation (LOPOCV) strategy was used to avoid autocorrelation between the training and evaluation dataset and therefore provided more insight into ABV mapping potential. The results showed



Academic Editor: Muhammad Moshiur Rahman

Received: 2 June 2026
Revised: 27 August 2026
Accepted: 28 August 2026
Published: 4 September 2026

that the combination of Sentinel-1 and Sentinel-2 features in the CNN model achieved the best predictive performance with $R^2$ and RMSE values of 0.64 and 0.39 $m^3 \cdot 100\ m^{-2}$, respectively. These findings highlight the potential of integrating multi-source information in advanced artificial intelligence algorithms for quinoa ABV monitoring, offering new insights toward the identification of sustainable practices across remote regions with complex socio-economic contexts.

**Keywords:** quinoa; aboveground biomass volume; Sentinel-1; Sentinel-2; machine learning; UAV

## 1. Introduction

### 1.1. Challenges in Agriculture Yield Monitoring

In the face of global food security challenges [1,2], the accurate estimation of crop yield is paramount for optimizing resource allocation, improving management practices, and ensuring economic viability [3]. Labor-intensive and destructive, traditional yield estimations are limited to small, uneven sample areas of a few square meters, from which yield is approximated at the field scale [4]. Such an approach is prone to significant uncertainties [4] as these observations are unable to capture intra-field yield variability related to intra-field soil fertility variability [5,6].

As an alternative, remote sensing data offer a non-invasive and scalable alternative that presents a promising avenue for enhancing yield monitoring [7–10]. For this purpose, yield sensitivity to satellite-based vegetation indices (i.e., NDVI) and climate evolution through the agricultural cycle (from sowing to harvest) is simulated in machine-learning models [11,12]. Although vegetation indices aim to capture intra-field variability (induced by soil fertility variability), these indices mainly represent the spectral response of the upper canopy layer [10,13]. Therefore, similar values may correspond to different crop structural conditions, particularly in dense canopies where index saturation occurs [14,15], avoiding the intra-field variability observation and leading to yield estimation uncertainties [16,17]. Similarly, the absence of detailed climatic observations at the intra-field level introduces additional uncertainty into predictive models [18]. Finally, it is worth mentioning that yield is not only sensitive to climate and soil fertility but also to edaphic factors (irrigation, use of fertilizers and/or pesticides) which change at intra- and especially inter-field scales. The omission of edaphic factors introduces serious inconsistencies and avoids model transferability in space and time.

### 1.2. Aboveground Biomass Volume as a Yield Proxy

Highly sensitive to (i) initial soil conditions, (ii) climate evolution, and (iii) the edaphic factors, the Aboveground Biomass Volume (ABV) appears as an ideal feature to integrate these factors and capture yield variability at the intra- and inter-field scale. Furthermore, for crops that bear their fruits/grains on the aerial part of the plant, ABV represents an excellent yield proxy [19], offering unprecedented opportunity to enhance yield monitoring [20,21]. In this context, several studies demonstrated the ability to monitor ABV using UAV imagery acquired in the Visible and Near Infra-Red (Vis–NIR) domain [22,23] or using LiDAR camera systems [24–27]. Despite the clear benefit of UAV imagery, these techniques imply specific fieldwork, thus preventing regional and retrospective monitoring. As an alternative scalable solution, the potential of Sentinel-1 (radar) and Sentinel-2 (Vis-NIR) satellite imagery for crop ABV monitoring has been assessed [28–32]. Using machine-learning models, studies across a wide range of agricultural systems compared single-sensor with combined-sensor approaches to estimate ABV [33–35]. The results show a clear complementarity of radar (Sentinel-1) and Vis-NIR (Sentinel-2) observations in improving ABV, particularly when crop structure and canopy density play a major role in ABV variability [35,36]. Nevertheless, as machine-learning models are highly sensitive to the representativeness and distribution of the calibration dataset, the reliability of this method is highly dependent on the quality, quantity, and spatial representativeness of the reference observations [37–39].

### 1.3. UAV and Satellite Synergy Opportunity

Gathering reference ABV observations at the coarse spatial resolution of satellite images (10 × 10 m) is almost out of reach due to (i) the superficial extent it represents (100 m square) and (ii) the difficulty to spatially match with the location of the corresponding satellite image grid-cells. In this context, reference ABV estimates are acquired on smaller spatial scales than the satellite spatial resolution and are therefore unable to reflect what the satellite actually observed. This spatial representativeness mismatch inevitably introduces uncertainties in the learning process; a well know issue affecting gridded climate dataset assessment based on uneven meteorological station observations [40,41]. Due to their reliability, UAV-based ABV estimates provide an effective alternative. Acquired at very high spatial resolution (i.e., a few cm), a simple upscale of UAV-based ABV estimates to the satellite spatial resolution will significantly improve the spatial representativeness and numbers of reference ABV observations. This will, in turn, improve the consistency of machine-learning model training, allowing satellite observations to be more effectively leveraged for large-scale operational monitoring.

### 1.4. Research Gap on Quinoa Monitoring

Over the last decades, quinoa has garnered significant attention due to its nutritional benefits and adaptability to diverse environmental conditions [42]. Consequently, a significant increase in quinoa crop extent driven by rising global demand has been observed across the Altiplano region, putting its cultivation at serious risk of becoming unsustainable [43,44]. Despite its key role in Altiplano economic and food security, quinoa monitoring remains underexplored and challenging due to the inherent heterogeneity in spatial coverage and development [45].

Most studies on quinoa have focused on crop mapping [45], phenotyping [46,47], and property monitoring [48]. Despite its clear benefit for quinoa ABV monitoring, no studies have evaluated the potential of such UAV-based approaches across the Altiplano. However, a recent study lead across Japan demonstrated the potential of the UAV method (photogrammetry) for estimating quinoa ABVs across multiple growth stages [48,49]. Limited to UAV observations, this study confirms the potential of UAV-based quinoa ABV monitoring that could leverage satellite ABV regional-scale monitoring.

### 1.5. Study Objectives

In the above-described context, this study proposes the use of UAV-based quinoa ABV estimates as reference observations to increase both the number and spatial representativeness of reference observations to monitor quinoa ABVs from the combination of Sentinel-1 and Sentinel-2 images. To minimize the influence of model structure on prediction, several decision-tree-based machine-learning models (Random Forest-RF, Gradient Boosting-GB, and eXtreme Gradient Boosting-XGB) were considered, separately and in a stacking approach, along with a CNN-based machine-learning model (CNN). Considering the economic and food security sensitivity to quinoa crops, the Bolivian Altiplano region was selected as the study case.

## 2. Materials

### *2.1. Study Area*

This study took place across the central Altiplano region of the department of La Paz in Bolivia (Figure 1). The region has a semi-arid climate, with (i) an average annual rainfall of less than 400 mm $\cdot yr^{-1}$, most of which falls during the austral summer [50], (ii) an average temperature ranging from 4 °C to 8 °C [40] and (iii) a high evapotranspiration rate of about 1300 $mm^{-1}$ [51]. Agriculture is the primary economic activity and relies heavily on irrigation due to a significant water shortage. The main crops grown in the area are potato, quinoa, alfalfa, along with other crops such as broad beans and barley [45]. Quinoa (*Chenopodium quinoa Willd.*) is characterized by a high genetic diversity, with numerous local varieties adapted to different agroecological conditions of the Andes, including varieties such as Kurmi, Surumi, Chucapaca, Intinayra, Maniqueña and Blanquita, which differ in grain size, productivity, and tolerance to abiotic stress [52,53]. Among these, the Jacha Grano variety (locally known as "large grain quinoa") is widely cultivated in the Bolivian Altiplano due to its good adaptation to high-altitude semi-arid conditions, relatively high grain yield potential, and large seed size, which is highly valued in local and international markets [54,55]. In this context, this study focuses on five plots of the Jacha Grano quinoa variety, ranging from 0.36 to 1.89 ha (Table 1).

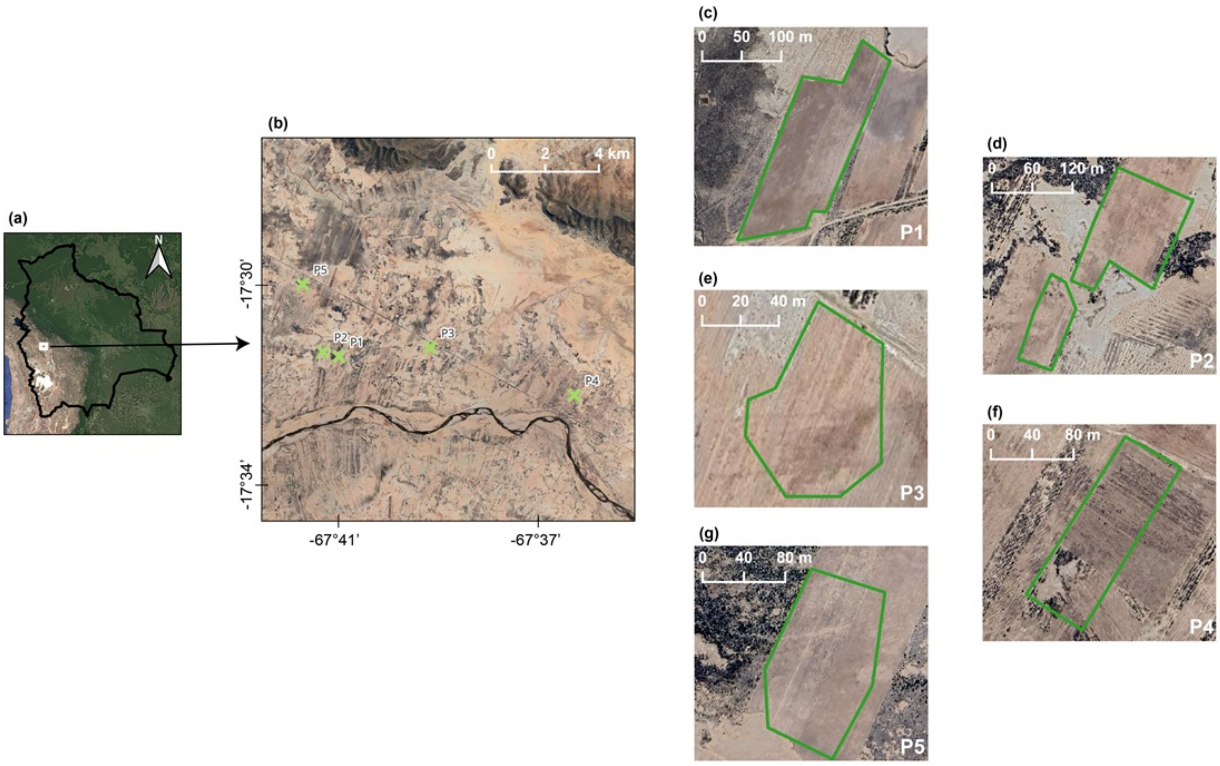


**Figure 1.** Location of the study area in Bolivia, (**a**) with the location of the five agricultural plots at the regional scale (**b**) and agricultural plot delineation in green (**c**–**g**).

**Table 1.** UAV flight dates with corresponding areas and S1 and S2 image acquisition dates.

| Plot | Date | Area (ha) | Number of Aerial Photographs | Date S1 | Date S2 |
|---|---|---|---|---|---|
| P1 | 30/04/25 | 1.34 | 336 | 15 and 27 April 2025 | 19, 22, 27 April 2025 |
| P2 | 30/04/25 | 1.89 | 546 | | |
| P3 | 30/04/25 | 0.36 | 130 | | |

**Table 1.** *Cont.*

| Plot | Date | Area (ha) | Number of Aerial Photographs | Date S1 | Date S2 |
|---|---|---|---|---|---|
| P4 | 09/05/25 | 0.88 | 291 | 27 April and 9 May 2025 | 27 April and 2, 7 May 2025 |
| P5 | 09/05/25 | 1.42 | 346 | | |

## 2.2. Reference Quinoa Aboveground Biomass Volume (ABV)

The reference ABV was obtained according to a four-step process, including (i) a photogrammetric process, (ii) Canopy Height Model (CHM) generation, (iii) crop area mapping, and finally (iv) ABV computation (Figure 2).

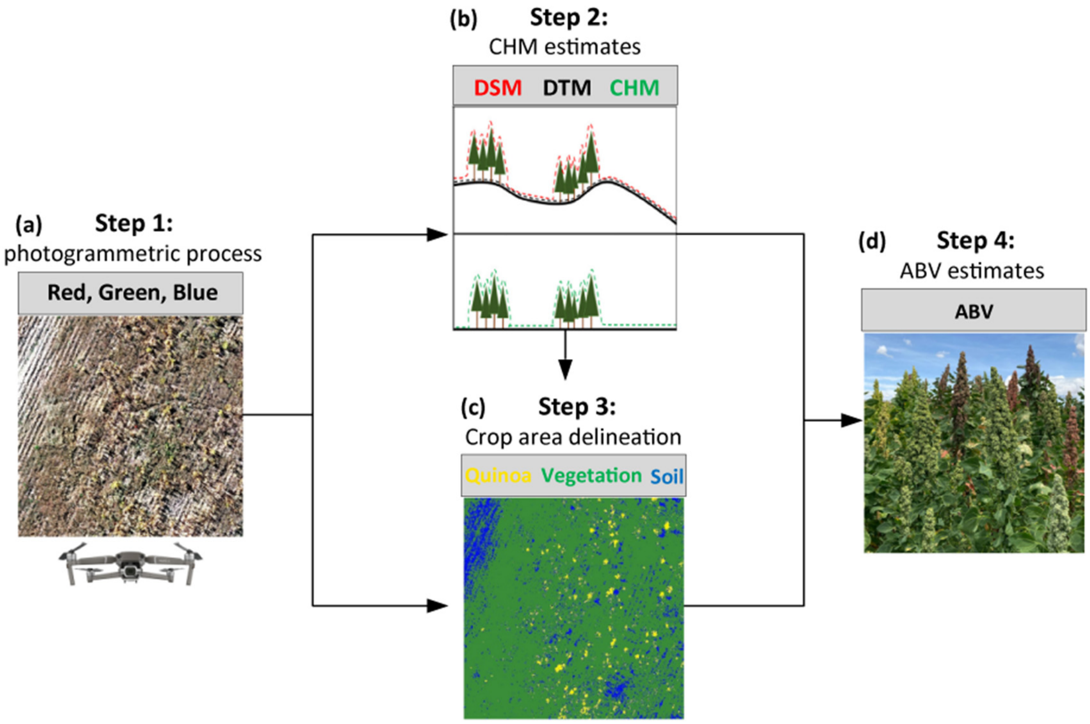


**Figure 2.** Four-step methodological approach based on UAV RGB images with the photogrammetric process (**a**), CHM estimates (**b**), crop area delineation (**c**) and ABV estimates (**d**).

First, high spatial resolution imagery was acquired over the five agricultural plots using a DJI Mavic 2 Pro UAV that comes with an RGB Hasselblad L1D-20C camera (28 mm focal length) and an onboard dual GNSS navigation system (GPS + GLONASS) for image geotagging and positioning. The UAV survey was lead during the grain-filling stage of quinoa development (April, May, Table 1), a period characterized by relatively stable canopy structure and biomass accumulation compared with earlier phenological stages. This approach aims to ensure (i) similar quinoa phenological development among the considered plots and (ii) strengthened consistency between UAV and satellite observations despite differences in acquisition dates.

As no RTK positioning or ground control points (GCPs) were available during the UAV surveys, image geo referencing relied on the onboard dual-GNSS system (Table 2). To mitigate potential geometric inconsistencies, image acquisition was planned in Pix4D Capture Pro at low altitude (30 m) with high image overlap (80%/70%) to ensure a ground sampling distance (GSD) of 0.7 cm · pixel$^{-1}$ (additional UAV flight mission and photogrammetric processing parameters are summarized in Table 2). The RGB images were processed in Agisoft Metashape v.1.2.7 software [56] using a photogrammetric workflow, including image alignment, dense point-cloud generation, digital surface model (DSM) and orthomosaic image reconstruction with acceptable uncertainties (Table 2). It is worth mentioning that photogrammetric products (DSM and RGB) were visually assessed to exclude areas affected by evident reconstruction distortions.

**Table 2.** UAV flight mission and photogrammetric processing parameters per plot.

| Parameter | P1 | P2 | P3 | P4 | P5 |
|---|---|---|---|---|---|
| UAV platform | DJI Mavic 2 Pro | | | | |
| Front/Side image overlap | 80%/70% | | | | |
| Camera angle | 90° | | | | |
| Coordinate system | WGS84/UTM Zone 19S (EPSG: 32719) | | | | |
| Flight altitude (m) | 26.4 | 36.8 | 36.1 | 31.1 | 32.6 |
| Ground sampling distance (GSD) (mm · pixel$^{-1}$) | 6.59 | 6.87 | 6.87 | 6.80 | 6.92 |
| Average XY camera location error (m) | 0.99 | 0.71 | 0.39 | 1.97 | 0.74 |
| Average Z camera location error (m) | 4.30 | 1.19 | 4.45 | 1.48 | 0.91 |
| Image reprojection error (pixel) | 0.57 | 0.66 | 0.51 | 0.56 | 0.58 |
| DSM resolution (cm · pixel$^{-1}$) | 1.32 | 1.37 | 1.37 | 1.36 | 1.38 |
| Orthomosaic resolution (mm · pixel$^{-1}$) | 6.91 | 6.87 | 6.87 | 6.80 | 6.91 |

Secondly, a Digital Terrain Model (DTM) was obtained interpolating ground points from the dense point-cloud, presenting a maximum terrain angle of 10° and a maximum distance of 0.1 m. Then, the CHM was obtained by subtracting the DTM from the DSM. This approach estimates canopy height relative to the local ground surface, providing a spatially explicit representation of crop structure suitable for deriving the ABV [57].

Thirdly, the CHM and RGB values were merged into a four-band raster using the DSM spatial resolution (Table 2). To improve its spatial consistency, the raster was geometrically aligned (co-registered) in QGIS 3.40 using high-resolution Google Earth imagery as a visual reference. This procedure was intended to reduce residual positional offsets associated with the onboard GNSS positioning while preserving the internal geometric consistency of the photogrammetric reconstruction [58–60]. Finally, the raster was classified into three land-cover classes (quinoa, soil, and vegetation) using a CNN model optimized using a gradient descent algorithm. In this process, the targets (quinoa, soil, and vegetation) were manually identified. The number of annotated samples were defined according to the structural complexity of each plot rather than its area (Table 3). Consequently, plots with greater heterogeneity or a lower proportion of quinoa plants required additional training samples to ensure adequate class representation and improve classification performance. Overall, the CNN achieved high classification performance, with accuracy values ranging from 86.2% to 93.4% (Table 3).

Fourth, the CHM was integrated with the classified raster to generate the volumetric space occupied by the quinoa canopy, which serves as a proxy for ABV. Finally, the ABV rasters were resampled to match S1 and S2 10-m spatial resolution, aggregating the ABV pixel values contained within each corresponding S1 and S2 grid-cell. The resulting maps revealed substantial spatial heterogeneity in the quinoa ABV, with values ranging from approximately 0 to 3.5 m$^3$ · 100 m$^{-2}$ (Figure 3). To better characterize this variability, the ABV was classified into five categories using the Jenks Natural Breaks (JNB) method, which optimizes class separation by minimizing within-class variance and maximizing between-class differences [61] (Figure 3).

**Table 3.** Training/testing sample numbers and performance metrics of the CNN classification model.

| Plot | Samples Training/Testing | Accuracy | Precision | Recall | F1-Score |
|---|---|---|---|---|---|
| P1 | 7288/3124 | 0.9046 | 0.9011 | 0.8980 | 0.8991 |
| P2 | 23,832/10,215 | 0.8993 | 0.8993 | 0.8925 | 0.8923 |
| P3 | 8308/3561 | 0.8624 | 0.8741 | 0.8271 | 0.8433 |
| P4 | 7704/3302 | 0.8795 | 0.8762 | 0.8691 | 0.8725 |
| P5 | 8575/3676 | 0.9336 | 0.9394 | 0.9293 | 0.9342 |

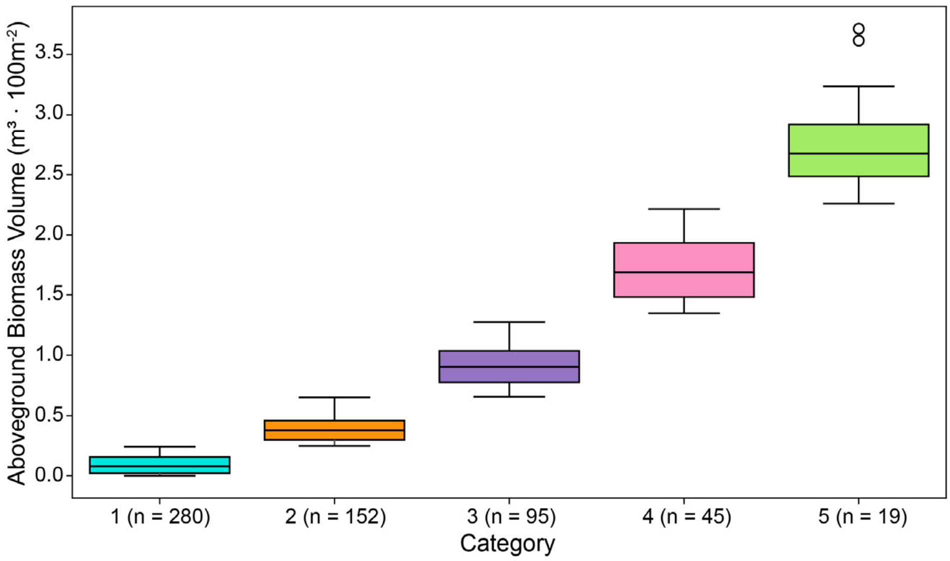


**Figure 3.** The distribution of measured ABV data.

### *2.3. Sentinel-2 Images and Pre-Processing*

Sentinel-2 (S2) images provides surface reflectance across 12 spectral bands covering the Vis-NIR region. In this study, bands B1 and B9 were excluded due to their coarse spatial resolution (60 m) and because they were primarily intended for water vapor and atmospheric corrections (aerosols and water vapor). S2 data are available before (Level-1C) and after (Level-2A) atmospheric correction. To guarantee temporal and spatial consistency in reflectance values, the atmospherically corrected Level-2A products were used. Cloud-affected pixels were detected with the "QA60" quality band and systematically masked as missing values. To minimize local noise and obtain representative site conditions, composite images were produced for each field campaign [5,62]. Each composite corresponds to the mean of three S2 images acquired during and immediately before the sampling date (Table 1). It is worth mentioning here that the composite images also aim to minimize the effects of crop phenological development, which can occur over short periods and potentially affect spectral reflectance.

Post-sampling images were excluded to avoid incorporating scenes captured after harvest. The S2 preprocessing steps (download and compositing) were performed in the Google Earth Engine [63] using the free Google Colab cloud platform (https://colab.research.google.com/, accessed on 15 May 2025).

### *2.4. Sentinel-1 Images and Pre-Processing*

Sentinel-1 (S1) images provide dual-polarization data in VV (vertical–vertical) and VH (vertical–horizontal) modes at a central frequency of 5.405 GHz in interferometric operation. Two main products are available: the Single Look Complex (SLC), which retains both amplitude and phase information, and the Ground Range Detected (GRD), which offers post-processed intensity images representing direct surface characteristics. Backscatter signals in VV, VH, or their combinations (such as VH/VV or RVI-type indices) allow for the estimation of key crop parameters (aboveground biomass, height, canopy density and structure, and surface soil moisture, even under partial cover), which are closely linked to potential productivity [64]. S1 scenes are acquired in both ascending and descending orbits; however, only descending passes were used to ensure spatial and temporal consistency. The pre-processing of S1 images comprised four sequential steps: (i) noise removal, (ii) radiometric calibration, (iii) topographic correction, and (iv) the application of a circular focal mean filter (50 m radius) to reduce speckle. As with the S2 composites, two S1 acquisitions closest to each sampling date were combined to lessen local noise effects (Table 1) and to minimize the effects of crop phenological development, which can affect the radar backscatter values.

In addition, the VV and VH backscatter coefficients expressed in dB were converted to linear $\sigma^0$ values and were subsequently used to derive eight polarization indices (PIs) and 36 texture indices (TIs). Texture metrics were computed using the Gray-Level Co-occurrence Matrix (GLCM) with a $5 \times 5$ moving window (size = 2) after scaling the linear backscatter values by 10,000 and converting them to 16-bit unsigned integers. The S1 workflow (download, pre-processing, and compositing) was implemented through the Google Earth Engine [63] using the free Google Colab platform (https://colab.research.google.com/, accessed on 15 May 2025).

### 2.5. Machine-Learning Models

Four decision-tree-based machine-learning models were evaluated: (i) Random Forest (RF) [65], (ii) Extreme Gradient Boosting (XGB) [66], (iii) Gradient Boosting (GB) [67] and (iv) Stacking models (STM), composed of the previously mentioned individual models. RF, GB, and XGB are non-parametric decision-tree-based models applicable to both regression and classification tasks. These algorithms use hierarchical tree-like structures to learn relationships between the input features and the target variable (i.e., ABV) [68]. RF extends this principle by constructing multiple trees from bootstrap samples of the training data (bagging), and averaging their outputs to obtain an ensemble prediction [65]. GB, in contrast, builds trees sequentially, with each new tree fitted to the residuals of the previous one to minimize a defined loss function [67]. XGB is an optimized implementation of GB that leverages parallelization and regularization to accelerate training and reduce overfitting [66]. The STM was considered due to its ability to provide more accurate and robust predictions than an individual model approach [69]. STM combines the predictions of multiple models (i.e., RF, GB or XGB) to exploit (reduce) the strengths (weaknesses) of their respective algorithms [69]. In this approach, the selected models are independently trained on the same dataset, and their predictions are then used as input features for a new model (meta-learner). The RF, GB and STM models were implemented with the scikit-learn library [70], whereas XGB was implemented using the xgboost package, which is compatible with scikit-learn [66]. In this process, the hyperparameters of each individual model (RF, GB and XGB) were tuned using the Grid Search algorithm for improving the performance of models [45].

A one-dimensional Convolutional Neural Network (CNN)-based machine learning model was considered to compare with decision-tree-based approaches. Unlike decision-tree-based models, CNNs automatically learn hierarchical and nonlinear feature representations through convolutional operations that capture local dependencies among predictor variables [71]. In a one-dimensional CNN architecture, successive convolutional layers

https://doi.org/10.3390/rs18173017

combined with pooling operations progressively reduce the dimensionality of the feature representations while retaining the most informative patterns, thereby improving feature abstraction and computational efficiency [72]. Additionally, batch normalization layers can be incorporated to stabilize and accelerate the training process by reducing internal covariate shift [73], whereas fully connected dense layers enable the integration of high-level features for continuous prediction of the target variable. The architecture also supports dropout regularization, which mitigates overfitting and improves model generalization by randomly deactivating neurons during training [74]. Finally, model optimization is commonly performed using adaptive optimization algorithms such as Adam, which dynamically updates network weights to improve convergence efficiency and predictive performance [75].

## 3. Methods

### *3.1. Learning Database*

S1 polarization (VV and VH) and S2 spectral reflectance (B2, B3, B4, B5, B6, B7, B8, B8a, B11, and B12) were extracted from all S1 and S2 composite images for the pixels contained in the five analyzed agricultural plots (n = 591). These data were subsequently used to derive 25 Spectral Indices (SIs) (Table 4), eight Polarization Indices (PIs), and 36 Texture Indices (TIs) (Table 5). The TIs were generated from the VV and VH linear backscatter coefficients using the GLCM approach described in Section 2.4. Following this process, the training database included 591 ABV observations with corresponding reflectance and polarization values, along with their associated SIs, PIs and TIs.

**Table 4.** Sentinel-2 features. Note that all indices were computed from the S2 composite image.

| N | Index/Acronym | Formula * or Description | Reference |
|---|---|---|---|
| 1 | Sentinel-2 bands | B2, B3, B4, B5, B6, B7, B8, B8A, B11, B12 | |
| 2 | Normalized Differential Vegetation Index (NDVI) | $\mathrm{NDVI} = \frac{\mathrm{NIR}-\mathrm{Red}}{\mathrm{NIR}+\mathrm{Red}}$ | [76] |
| 3 | Soil-Adjusted Vegetation Index (SAVI) | $\mathrm{SAVI} = \frac{\mathrm{NIR}-\mathrm{Red}}{\mathrm{NIR}+\mathrm{Red}+0.5} \times 1.5$ | [77] |
| 4 | Enhanced Vegetation Index (EVI) | $\mathrm{EVI} = 2.5 \times \frac{\mathrm{NIR}-\mathrm{Red}}{\mathrm{NIR}+6\times\mathrm{Red}-7.5\times\mathrm{Blue}+1}$ | [78] |
| 5 | Normalized Difference Moisture Index (NDMI) | $\mathrm{NDMI} = \frac{\mathrm{NIR}-\mathrm{SWIR1}}{\mathrm{NIR}+\mathrm{SWIR1}}$ | [76] |
| 6 | Moisture Stress Index (MSI1) | $\mathrm{MSI1} = \frac{\mathrm{SWIR1}}{\mathrm{NIR}}$ | [79] |
| 7 | Moisture Stress Index (MSI2) | $\mathrm{MSI2} = \frac{\mathrm{SWIR1}-\mathrm{NIR}}{\mathrm{SWIR1}+\mathrm{NIR}} \times \frac{\mathrm{SWIR1}-\mathrm{Red}}{\mathrm{SWIR1}+\mathrm{Red}}$ | Modified from [76] |
| 8 | Bare Soil Index (BSI) | $\mathrm{BSI} = \frac{(\mathrm{Red}+\mathrm{SWIR1})-(\mathrm{NIR}+\mathrm{Blue})}{(\mathrm{Red}+\mathrm{SWIR1})+(\mathrm{NIR}+\mathrm{Blue})}$ | [80] |
| 9 | Normalized Burn Ratio (NBR) | $\mathrm{NBR} = \frac{\mathrm{NIR}-\mathrm{SWIR2}}{\mathrm{NIR}+\mathrm{SWIR2}}$ | [81] |
| 10 | Normalized Burn Ratio 2 (NBR2) | $\mathrm{NBR2} = \frac{\mathrm{SWIR1}-\mathrm{SWIR2}}{\mathrm{SWIR1}+\mathrm{SWIR2}}$ | [82] |
| 11 | Normalized Difference Water Index (NDWI) | $\mathrm{NDWI} = \frac{\mathrm{NIR}-\mathrm{Green}}{\mathrm{NIR}+\mathrm{Green}}$ | [83] |
| 12 | Normalized Salinity Index (NSI1) | $\mathrm{NSI1} = \frac{\mathrm{SWIR1}-\mathrm{SWIR2}}{\mathrm{SWIR1}+\mathrm{NIR}}$ | [84] |
| 13 | Modified Normalized Salinity Index (NSI2) | $\mathrm{NSI2} = \frac{\mathrm{SWIR1}-\mathrm{SWIR2}}{\mathrm{SWIR1}-\mathrm{NIR}}$ | Modified from [84] |
| 14 | Normalized Difference Salinity Index (NSI) | $\mathrm{NDSI} = \frac{\mathrm{Green}-\mathrm{Red}}{\mathrm{Green}+\mathrm{Red}}$ | [85] |
| 15 | Salinity index 1 (SI1) | $\mathrm{SI1} = \sqrt{\mathrm{Red} \times \mathrm{Green}}$ | [86] |
| 16 | Salinity index 2 (SI2) | $\mathrm{SI2} = \sqrt{\mathrm{Blue} \times \mathrm{Red}}$ | [87] |
| 17 | Salinity index 3 (SI3) | $\mathrm{SI3} = \sqrt{\mathrm{Red}^2 \times \mathrm{Green}^2}$ | [87] |
| 18 | Salinity index 4 (SI4) | $\mathrm{SI4} = \frac{\mathrm{NIR}\times\mathrm{SWIR1}-\mathrm{SWIR1}^2}{\mathrm{NIR}}$ | [84] |
| 19 | Salinity index 5 (SI5) | $\mathrm{SI5} = \frac{\mathrm{Blue}}{\mathrm{Red}}$ | [87] |
| 20 | Salinity index 6 (SI6) | $\mathrm{SI6} = \frac{\mathrm{Red}\times\mathrm{NIR}}{\mathrm{Green}}$ | [87] |
| 21 | Vegetation Soil Salinity Index (VSSI) | $\mathrm{VSSI} = 2 \times \mathrm{Green} - 5 \times (\mathrm{Red} + \mathrm{NIR})$ | [88] |

**Table 4.** *Cont.*

| N | Index/Acronym | Formula * or Description | Reference |
|---|---|---|---|
| 22 | Normalized Difference Salinity Index (NSI) | $NSI = \frac{Red-NIR}{Red+NIR}$ | [85] |
| 23 | Salinity Ratio (SR) | $SR = \frac{Green-Red}{Blue+Red}$ | [88] |
| 24 | Canopy Response Salinity Index (CRSI) | $CRSI = \sqrt{\frac{NIR\times Red-Green\times Blue}{NIR\times Red+Green\times Blue}}$ | [84] |
| 25 | Brightness Index (BI1) | $BI1 = \sqrt{Red^2 + NIR^2}$ | [89] |
| 26 | Brightness Index (BI2) | $BI2 = \sqrt{Green^2 + Red^2 + NIR^2}$ | [86] |

* Where Blue = B2; Green = B3; Red = B4; NIR = B8; SWIR1 = B11; SWIR2 = B12.

**Table 5.** Sentinel-1 features. Note that all indices were computed from the S1 composite image.

| N | Index/Acronym | Formula * or Description | Reference |
|---|---|---|---|
| | Sentinel-1 polarization (dB) | VV, VH | |
| 1 | Polarization index 1 (PI1) | $PI1 = VV + VH$ | [90] |
| 2 | Polarization index 2 (PI2) | $PI2 = VV^2 + VH$ | |
| 3 | Polarization index 3 (PI3) | $PI3 = VH^2 - VV$ | |
| 4 | Polarization index 4 (PI4) | $PI4 = VV^2 + VH^2$ | |
| 5 | Polarization index 5 (PI5) | $PI5 = \frac{VV^2+VH^2}{VH}$ | |
| 6 | Polarization index 6 (PI6) | $PI6 = Log(VV) * 10$ | |
| 7 | Polarization index 7 (PI7) | $PI7 = Log(VH) * 10$ | |
| 8 | Polarization index 8 (PI8) | $PI8 = (Log(VV) + Log(VH)) * 10$ | |
| 9 | Textural index (Extracted from VV and VH Band)<br>Angular second moment (asm)<br>Contrast (contrast)<br>Correlation (corr)<br>Variance (var)<br>Inverse difference moment (idm)<br>Sum average (savg)<br>Sum variance (savr)<br>Sum entropy (sent)<br>Entropy (ent)<br>Difference variance (dvar)<br>Difference entropy (dent)<br>Information measure of correlation 1 (imcorr1)<br>Information measure of correlation 2 (imcorr2)<br>Maximum correlation coefficient (maxcorr)<br>Dissimilarity (diss)<br>Inertia (inertia)<br>Shade (shade)<br>Cluster prominence (prom) | <br>VV asm, VH asm<br>VV contrast, VH contrast<br>VV corr, VH corr<br>VV var, VH var<br>VV idm, VH idm<br>VV savg, VH savg<br>VV svar, VH svar<br>VV sent, VH sent<br>VV ent, VH ent<br>VV dvar, VH dvar<br>VV dent, VH dent<br>VV imcorr1, VH imcorr1<br>VV imcorr2, VH imcorr2<br>VV maxcorr, VH maxcorr<br>VV diss, VH diss<br>VV inertia, VH inertia<br>VV shade, VH shade<br>VV prom, VH prom | [91–93] |

* Where VV = Vertical transmission/Vertical reception; VH = Vertical transmission/horizontal reception.

Considering the low surface coverage of quinoa plants (Figure 1c), the spectral signal captured by satellites at a 10 m spatial resolution was expected to be sensitive to both vegetation and soil conditions. In this context, Vis-NIR indices not directly related to the vegetation condition were included to account for soil background effects. For specific indices related to salinity and soil moisture, their inclusion was further justified by the sensitivity of quinoa to soil salinity and moisture, which are generally high and low, respectively, across the Altiplano [5,6]. Finally, the inclusion of several soil salinity and textures indices aimed to account for the model-specific sensitivity of machine-learning algorithms to input features. Indeed, previous studies on crop-type, soil salinity, and soil moisture mapping have shown that feature importance varies substantially depending on the model considered [5,6,45]. In this context, including several indices helps to avoid potential reductions in model performance resulting from the exclusion of features that may be relevant for specific models [45].

### *3.2. Modelling Set-Up and Performance Assessment*

To assess ABV sensibility to radar (S1) and Vis-NIR (S2) signals, three scenarios were evaluated for each of the five considered models (RF, GB, XGB, STM and CNN) (Figure 4). The first scenario (Scenario-1) incorporated only S2-derived features, the second scenario (Scenario-2) used exclusively S1-derived features, the third scenario (Scenario-3) combined both S1 and S2 feature sets. This experimental design enabled the independent evaluation of Vis-NIR and radar information, as well as their combined contributions to ABV estimation.

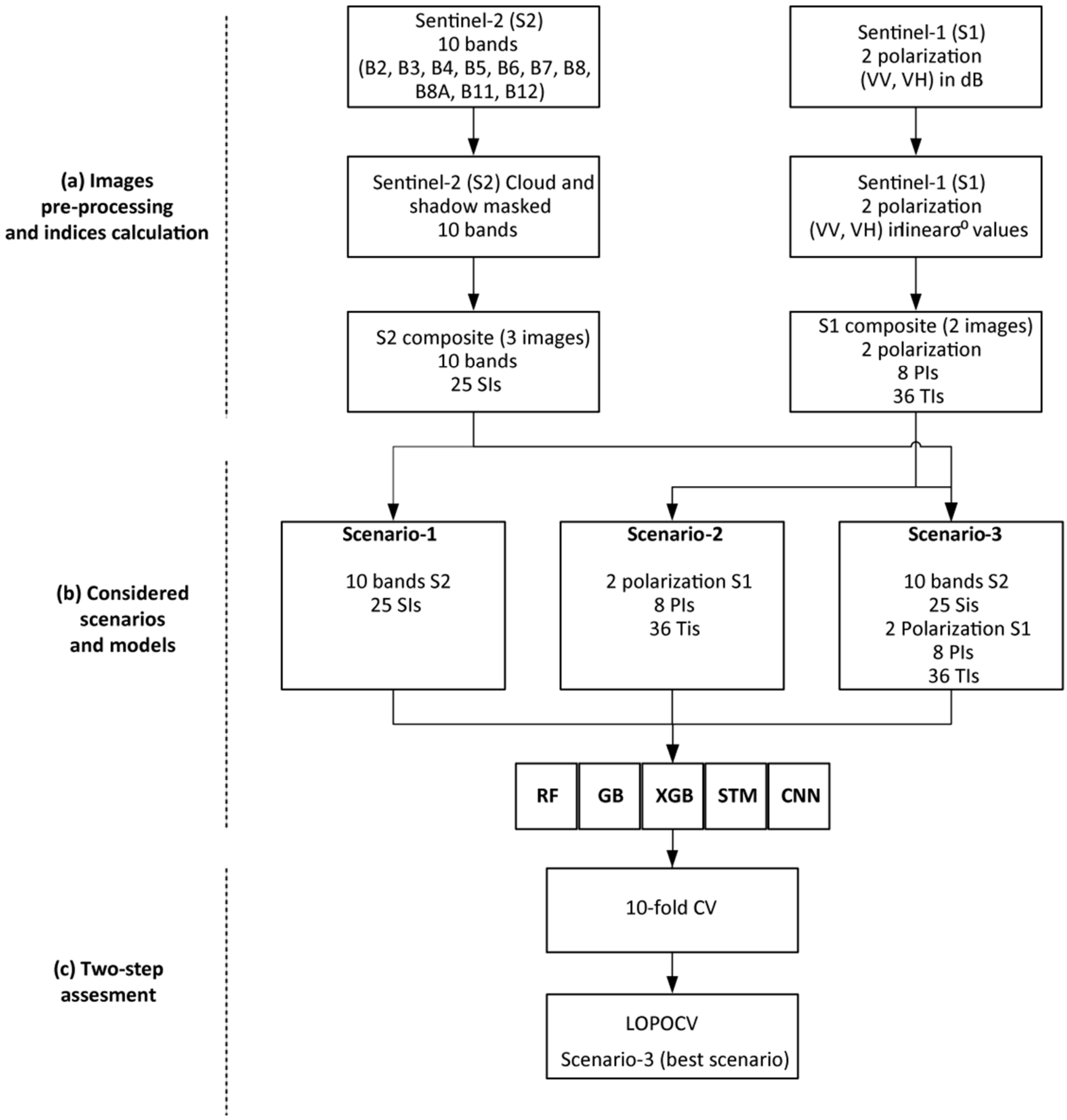


**Figure 4.** ABV modeling flowchart showing S1 and S2 pre-processing and indices calculations, (**a**) the considered models and scenarios (**b**) and the two-step assessment, including 10-fold and LOPO cross validation (**c**).

As detailed in Section 2.5, the hyperparameters of the RF, GB, and XGB models were tuned using the Grid Search algorithm to improve their predictive performance. The STM configuration was implemented by integrating the predictions generated by the RF, GB, and XGB models through a meta-learner trained on the same input dataset. For the CNN model, the architecture consisted of three consecutive Conv1D layers with 32, 64, and 128 filters, respectively, using a kernel size of 3, a stride of 2, ReLU activation functions, and the same padding. Batch normalization and MaxPooling1D layers were incorporated after the first two convolutional blocks, whereas the extracted feature maps were flattened and connected to three fully connected dense layers with 128, 64, and 32 neurons, respectively. To reduce overfitting, a dropout layer with a rate of 0.3 was applied before the final output neuron. Model training was performed using the Adam optimizer, with a learning rate of 0.001 and a mean squared error (MSE) loss function. Additionally, an early stopping strategy was implemented to improve model generalization and predictive robustness.

The predictive performance of the models (RF, GB, XGB, STM and CNN) under the three proposed scenarios was evaluated using a 10-fold cross-validation strategy. For each iteration, the dataset was randomly partitioned into ten equally sized subsets, where nine subsets were used for training and the remaining subset was used for validation. This process was repeated until each subset had served once as validation data, ensuring that all observations participated in both training and validation phases. Final performance statistics correspond to the average values obtained across all cross-validation iterations. Model accuracy and reliability were quantified using the coefficient of determination ($R^2$, Equation (1)) and the root mean square error (RMSE, Equation (2)).

$$R^2 = 1 - \frac{\sum_{i=1}^{n} (P_i - \overline{O})^2}{\sum_{i=1}^{n} (O_i - \overline{O})^2} \quad (1)$$

$$RMSE = \sqrt{\frac{1}{n}\sum_{i=1}^{n} (P_i - O_i)^2} \quad (2)$$

where n denotes the total number of samples and Pi and Oi represent the predicted and observed ABV values at site i, respectively.

### 3.3. ABV Mapping to Assess the Models' Spatial Transferability

In spatial remote sensing applications, conventional random validation approaches, such as the *k*-fold cross-validation, may produce overly optimistic accuracy estimates because training and validation samples are often spatially autocorrelated. Actually, neighboring observations share similar environmental and spectral characteristics, increasing the likelihood that the validation set contains samples highly correlated with those used for training. Consequently, model performance may reflect the interpolation of nearby observations rather than the true ability to generalize to new locations [94,95]. Group-based validation strategies, such as Leave-One-Group-Out (LOGO) or Leave-One-Plot-Out (LOPO), overcome this limitation by assigning all observations from the same spatial unit to either the training or validation set, thereby preserving spatial independence between both datasets. Such approaches provide a more realistic assessment of model transferability and are therefore recommended for machine-learning applications involving spatially clustered or field-based observations [94–96].

In this context, considering the best-performing scenario, the Leave-One-Plot-Out Cross-Validation (LOPOCV) strategy was used to assess the models' spatial transferability under independent validation conditions [95]. To do so, the models were trained excluding the data corresponding to the plot that would subsequently be mapped. As five plots are under consideration, this operation was retired five times. Then, the five generated

ABV maps were compared to the one observed by the UAV and the associated uncertainty calculated through the $R^2$ and RMSE.

# 4. Results

## 4.1. Model Performance

ABV variability was successfully captured by all models across the three scenarios. Overall, the integration of radar and Vis-NIR features (Scenario-3) consistently produced the highest predictive performance, highlighting the complementary contribution of S1 and S2, respectively. Considering Scenario-3, the CNN model showed the highest predictive performance, with $R^2$ and RMSE values of 0.64 and 0.39 $m^3 \cdot 100\ m^{-2}$, respectively (Table 6). However, its performance was only marginally better than that of the RF model, which exhibited $R^2$ and RMSE values of 0.62 and of 0.4 $m^3 \cdot 100\ m^{-2}$, respectively, followed by the XGB ($R^2$ = 0.60; RMSE = 0.41 $m^3 \cdot 100\ m^{-2}$) and GB ($R^2$ = 0.59 and RMSE = 0.41 $m^3 \cdot 100\ m^{-2}$). The STM model showed comparatively lower performance under Scenario-3 ($R^2$ = 0.58; RMSE = 0.41 $m^3 \cdot 100\ m^{-2}$), although it maintained competitive results when only Vis-NIR variables (secenario-1) were considered (Table 6).

**Table 6.** Model performance obtained with 10-fold cross-validation.

| Model | Metrics | Scenario-1 Vis-NIR | Scenario-2 Radar | Scenario-3 Vis-NIR + Radar |
|---|---|---|---|---|
| RF | $R^2$ | 0.59 | 0.53 | 0.62 |
| | RMSE ($m^3 \cdot 100\ m^{-2}$) | 0.41 | 0.44 | 0.40 |
| GB | $R^2$ | 0.57 | 0.54 | 0.59 |
| | RMSE ($m^3 \cdot 100\ m^{-2}$) | 0.42 | 0.44 | 0.41 |
| XGB | $R^2$ | 0.57 | 0.54 | 0.60 |
| | RMSE ($m^3 \cdot 100\ m^{-2}$) | 0.42 | 0.43 | 0.41 |
| STM | $R^2$ | 0.59 | 0.53 | 0.58 |
| | RMSE ($m^3 \cdot 100\ m^{-2}$) | 0.41 | 0.44 | 0.41 |
| CNN | $R^2$ | 0.56 | 0.55 | 0.64 |
| | RMSE ($m^3 \cdot 100\ m^{-2}$) | 0.43 | 0.43 | 0.39 |

The scatter plots further demonstrate that considering Vis-NIR and radar information (Scenario-3) produced predictions closer to the 1:1 reference line (particularly for intermediate and high ABVs) between observed and predicted ABV values (Figure 5). In contrast, models trained exclusively with radar variables (Scenario-2) exhibited lower predictive performance, suggesting that S1 information alone was less effective in representing ABV variability. Despite the overall satisfactory predictive performance, all models showed a tendency to underestimate extreme ABV values, especially at the upper range of observed ABV values.

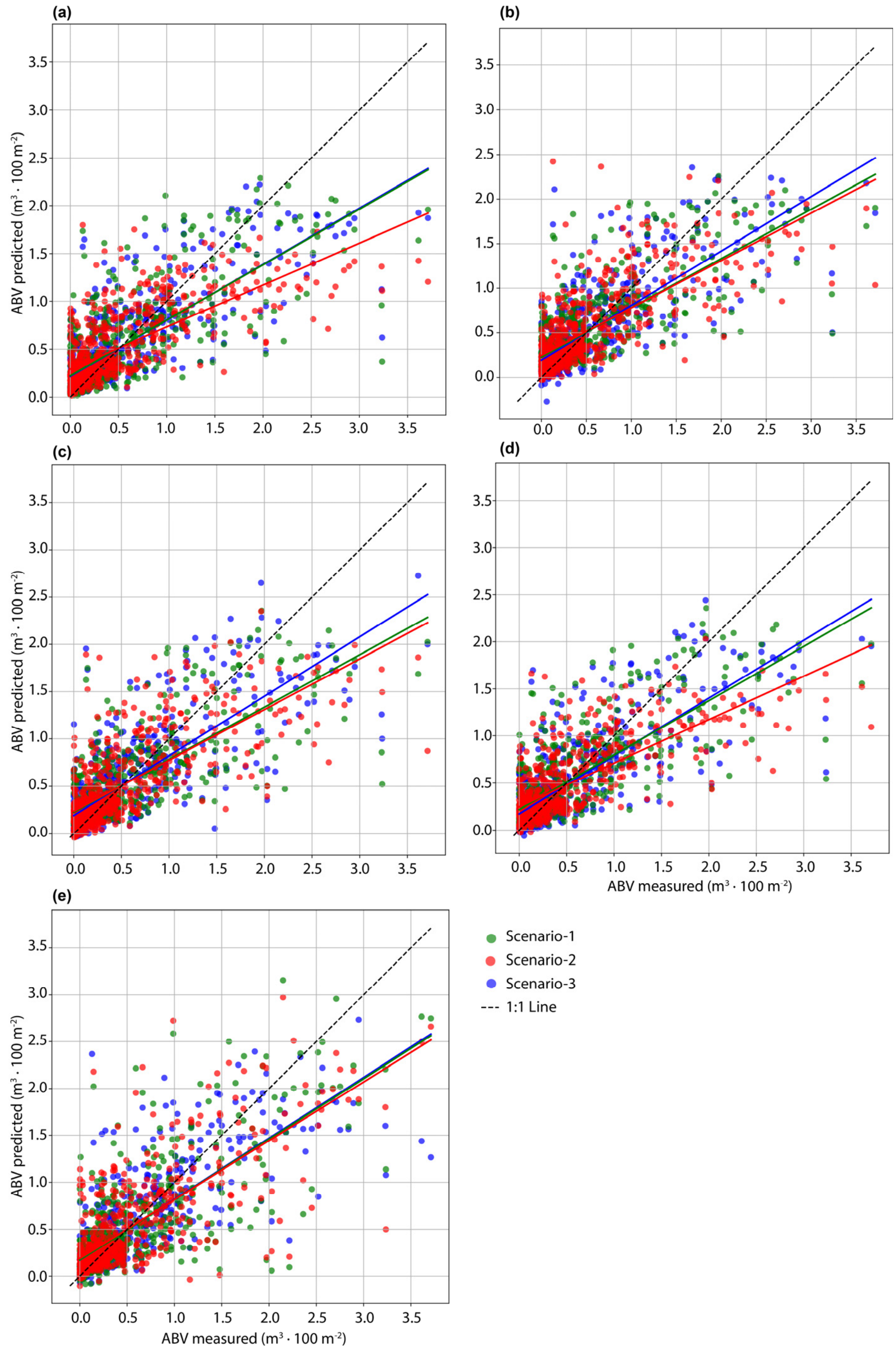


**Figure 5.** Scatterplots for the different scenarios and models: RF (**a**), GB (**b**), XGB (**c**), STM (**d**) and CNN (**e**).

## *4.2. ABV Mapping*

The spatial distribution of reference ABV in quinoa plots revealed important differences among the considered models in their ability to reproduce field-scale heterogeneity (Figure 6). All models (RF, GB, XGB, STM and CNN) captured the general spatial trends of ABV variability. Despite their general robustness, especially under limited training data and computationally efficiency, ensemble-based models such as RF and STM generated smoother patterns and underestimated localized zones of high and low ABVs (Figure 5a,d). In contrast, CNN showed a greater capacity to preserve fine-scale spatial patterns and abrupt transitions between the ABV classes, particularly in highly heterogeneous plots (Figure 5e). This improvement is likely associated with the ability of CNN architectures to incorporate spatial autocorrelation and contextual information among neighboring pixels [97], which are critical characteristics in ABV mapping.

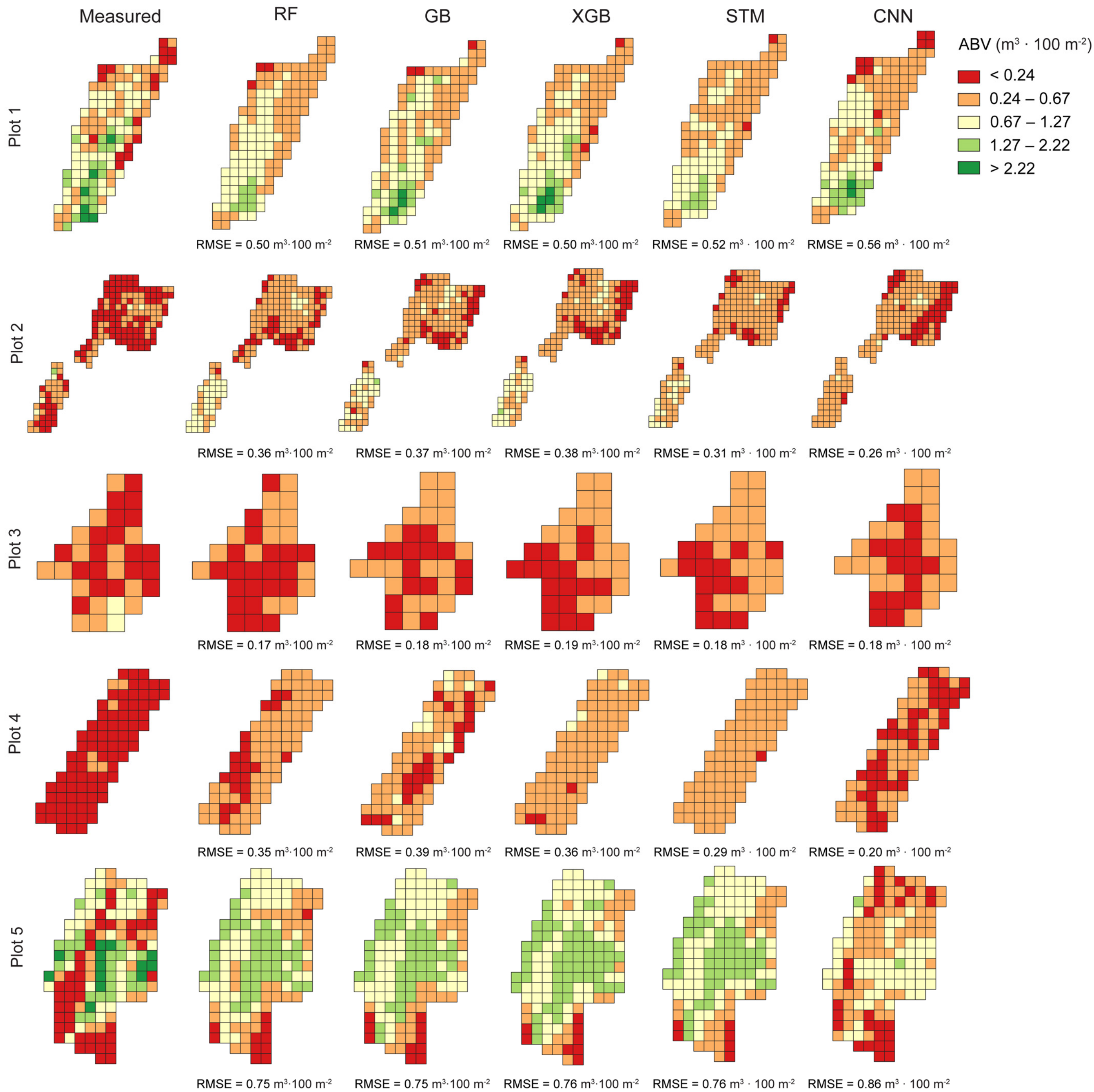


**Figure 6.** ABV mapping per plot using the observed UAV-derived ABV (**left**) and the predictions of the five models under Scenario-3 (**right**).

The results also demonstrate that model performance varied according to the structural complexity and heterogeneity of the plots. Using the combined S1 and S2 dataset (Scenario-3), all models produced similar ABV distributions in relatively homogeneous plots (Figure 6—plots 2–4), whereas in plots with greater spatial variability (Figure 6—plots 1 and 5), CNN and, to a lesser extent, boosting algorithms (GB and XGB), more accurately reproduced the observed patterns. This visual assessment is consistent with the RMSE values obtained for each plot, which were generally low, ranging from 0.17 to 0.86 $m^3{\cdot}100\ m^{-2}$ across all models. Such relatively low RMSE values indicate a limited degree of discrepancy between predicted and observed ABV values, suggesting that the models provided overall acceptable reliability. Furthermore, lower RMSE values observed in plots 2–4 reinforced the ability of the models to accurately characterize more homogeneous conditions, whereas the slightly higher errors in plots 1 and 5 reflect the greater challenge of reproducing highly heterogeneous spatial patterns.

It is worth mentioning here that the LOPOCV was designed to evaluate the ability of the models to generalize to an entirely unseen agricultural plot. Thus, the results obtained for each plot should not be interpreted only as within-plot predictive performance, but also as an assessment of model transferability to spatially independent conditions not represented during model training. Despite the limited number of considered plots (n = 5), the LOPOCV strategy adopted here highlights the potential for model transferability across unseen regions.

## 5. Discussion

### 5.1. UAV-Based Photogrammetric Estimation of ABV

Due to their low cost and high spatial resolution, UAVs have previously been used to retrieve ABV estimation in both herbaceous and agricultural crops (including quinoa) using similar photogrammetry-based approaches [48,49].

However, photogrammetry has limitations in cover areas with complex architecture, the presence of shadows, or sparse vegetation, so that 3D reconstruction can lose accuracy. In this context, the integration of airborne LiDAR sensors could significantly improve the quality of ABV estimates due to their ability to directly capture the three-dimensional structure of the crop and partially penetrate the vegetation canopy [98,99]. Actually, recent studies report that LiDAR sensors provide more accurate height models and structural metrics than conventional photogrammetry, improving the estimation of ABV and biophysical parameters of the crop [100]. Furthermore, the synergistic combination of LiDAR and photogrammetry has shown promising results by integrating the geometric precision of LiDAR with the high spectral resolution of optical images and red-edge vegetation indices [29,101]. In the present study, the discrepancies observed in low ABV plots suggest that part of the uncertainty may be associated with the limited capacity to accurately discriminate quinoa plants from other ground cover components, such as weeds, crop residues, and bare soils. Actually, spectral confusion between crops and surrounding vegetation affects ABV estimation accuracy, particularly under sparse or heterogeneous canopy conditions [15]. In this context, the use of UAVs equipped with multispectral or hyperspectral sensors will provide detailed spectral signatures and substantially improve the spectral differentiation of plant species and crop delineation [102,103].

Finally, additional ABV uncertainties could emerge from the lack of RTK positioning or Ground Control Points (GCPs). However, in this study, the CHM was generated from the difference between the DSM and DTM derived from the same photogrammetric reconstruction, which partially compensates for systematic georeferencing errors. In addition, the sparse canopy structure of quinoa facilitates ground-point identification, enabling the estimation of relative CHM above the surrounding terrain rather than relying on absolute terrain elevation. Similar approaches have been successfully applied for estimating crop height, canopy volume, and biomass without requiring centimetric absolute positioning accuracy [104–106].

### 5.2. Temporal Constraints and Regional Applicability

In this study, the reference ABV observations were derived during the grain-filling stage of quinoa development (April, May) and across a limited field number (n = 5). Consequently, the proposed models were calibrated and evaluated under relatively stable canopy conditions and do not explicitly account for temporal and spatial variations in crop structure and biomass accumulation throughout the growing season and at the inter-field scale. Previous studies have shown that the relationships between remote sensing variables and biomass vary across phenological stages, owing to changes in canopy architecture, vegetation cover, leaf area, and vegetation water content, which directly influence both Vis-NIR reflectance and radar backscatter [33,105,107,108]. Likewise, multi-temporal observations have consistently been shown to improve biomass estimation by capturing crop growth dynamics throughout the season [109,110]. Therefore, future research should incorporate multi-temporal UAV and satellite observations acquired from crop emergence to harvest to improve the temporal and spatial stability of the proposed models in the scope of season-long and regional crop monitoring.

### 5.3. Complementarity Between Radar and Vis-NIR Data for ABV Monitoring

The results show that integrating S1 and S2 systematically outperformed the individual sensor due to the complementary nature of C-band SAR and Vis-NIR data for crop ABV estimation.

Sentinel-2 Vis-NIR imagery primarily captures the biochemical and physiological characteristics of vegetation, including chlorophyll content, leaf area, and canopy vigor, through spectral reflectance and vegetation indices [111,112]. In contrast, Sentinel-1 C-band SAR observations are sensitive to crop structural properties, canopy architecture, surface roughness, and vegetation water content, while maintaining acquisition capability under cloudy conditions and varying illumination [113–115]. Consequently, the fusion of both sensors provides complementary information describing both the spectral and structural characteristics of the crop, thereby reducing the limitations associated with single-sensor approaches, such as optical saturation under dense canopies or the limited sensitivity of C-band SAR at advanced biomass levels. This complementary behavior has consistently been reported to improve biomass estimation and crop monitoring across different agricultural systems using machine-learning approaches [33,45,116–118].

### 5.4. Limit of the Proposed Method for High ABV

An underestimation of ABV in plots exhibiting the highest biomass values was observed. This behavior is commonly observed in remote sensing-based biomass estimation and can be attributed to several complementary factors. First, Vis-NIR vegetation indices tend to saturate under dense canopy conditions, reducing their sensitivity to additional biomass accumulation once high vegetation cover is reached [14,119]. Although the integration of S1 partially alleviates this limitation by incorporating structural information, C-band SAR backscatter may also exhibit reduced sensitivity at high biomass levels due to signal saturation and multiple scattering effects within dense canopies [33,114,120]. Second, the learning database contained relatively few observations within the highest ABV range, limiting the ability of the considered models to learn "extreme" biomass conditions. Under such circumstances, the models tend to produce conservative predictions biased towards the central portion of the response distribution, resulting in the underestimation of extreme values [38,121]. These findings suggest that future studies should increase the representation of high-biomass observations and incorporate multi-temporal measurements spanning different crop development stages to improve model calibration across the full range of ABV conditions.

### 5.5. Feature Selection and Model Complexity

In remote sensing applications characterized by high-dimensional datasets containing large numbers of spectral, textural, and derived variables, feature selection is generally employed to reduce redundancy, eliminate irrelevant information, and minimize overfitting [45,122]. In the present study, feature selection was not applied because the dataset exhibited a low-dimensional structure, where the number of observations substantially exceeded the number of predictor variables. Under these conditions, the risk of the "curse of dimensionality" and model overfitting associated with high-dimensional feature spaces is considerably reduced [121]. In deep-learning architectures such as CNN, feature selection is implicitly performed during the training process, enabling the model to learn hierarchical representations and complex nonlinear relationships directly from the complete set of input variables [71,123]. Consequently, prior feature selection may limit the model's ability to identify relevant high-level patterns and variable interactions. Similarly, in ensemble machine-learning approaches, feature selection may disproportionately favor the performance of certain individual algorithms, since each model exhibits different sensitivities to input features and variable distributions [124]. This may reduce the internal diversity of the ensemble and introduce biases toward variables preferred by specific algorithms, thereby affecting the complementarity of models, which constitutes one of the principal strengths of ensemble learning. Therefore, maintaining the complete set of variables may provide a more robust representation of the spectral and spatial variability present in the data, particularly in complex precision agriculture and ABV estimation applications.

### *5.6. ABV as a Proxy for Quinoa Yield*

Although the present study focused on estimating ABV, the ultimate objective of precision agriculture is generally the prediction of crop yield. In this study, yield observations were not available for all agricultural plots and therefore were not incorporated into the machine-learning framework. Nevertheless, despite the ABV distribution being biased toward low values, preliminary field measurements (n = 10) indicated a consistent linear relationship between the reference ABV (observed by UAV) and quinoa yield (measured over a four-square-meter area) ($R^2$ = 0.91, Figure 7), suggesting that ABV may provide a reliable proxy for final grain production under the studied conditions. Similar relationships between crop structural attributes derived from UAV imagery and yield have been reported for several agricultural crops, where canopy height and volume effectively integrate the cumulative effects of crop growth throughout the season [19,105,125,126].

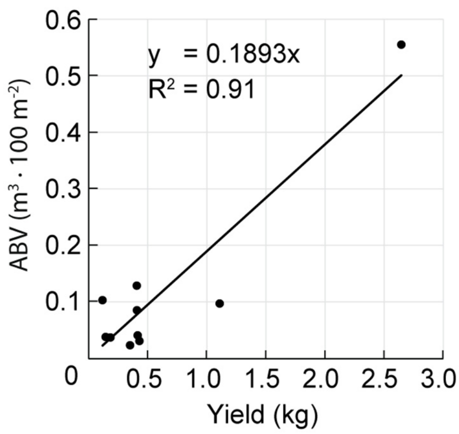


**Figure 7.** Relationship between ABV and quinoa yield.

In this context, future studies should prioritize additional field yield sampling to strengthen the observed relationship between ABV and yield to develop end-to-end predictive models capable of directly estimating crop productivity from UAV and/or Sentinel observations. Such an approach would provide practical value for precision agriculture by supporting field-scale yield forecasting and management decisions.

https://doi.org/10.3390/rs18173017

## 6. Conclusions

This study assessed the integration of several remote sensing datasets (i.e., Sentinel-1, Sentinel-2 and UAV RGB) in advanced machine-learning techniques for quinoa Above-ground Biomass Volume (ABV) mapping at high spatial resolution (10 m). For this task, several decision-tree-based machine-learning models (Random Forest—RF, Extreme Gradient Boosting—XGB and Gradient Boosting—GB) were considered separately and according to a stacking approach (STM), along with a Convolutional Neural Network-based machine-learning model (CNN) for comparison. The key findings can be summarized as follows:

- Photogrammetry applied to UAV RGB images is an efficient alternative to traditional destructive sampling to retrieve reference ABV observations, as it increases the number of observations and the spatial consistency between reference ABV and satellite observations.
- More consistent ABV estimates are obtained using both Sentinel-2 and Sentinel-1 images rather than using these data sources alone, highlighting the complementarity of Vis-NIR and radar data.
- Among the considered models, CNN provides the most accurate ABV estimates ($R^2$ = 0.64, RMSE = 0.39), outperforming all machine-learning models (RF, XGB, GB) separately or according to a stacking approach (STM).
- Quinoa ABV mapping revealed high spatial heterogeneity within the analyzed plots, which cannot be captured except with a high-spatial-resolution remote sensing-based monitoring technique, such as the one introduced in this study.

Although the proposed method focuses on ABV monitoring, future studies should focus on its transfer towards quinoa crop yield estimates. Actually, quinoa bears its grains on the upper part of the plant, and a strong relationship between quinoa ABV and yield is expected. Once the relationship between quinoa ABV and yield is clearly established, remote sensing ABV estimates may contribute to future operational monitoring systems aimed at supporting agricultural management and food-security assessments. In this context, evaluating the scalability and transferability of these approaches across different crop types and larger agricultural landscapes could further strengthen the applicability of multisource remote sensing and advanced machine-learning techniques as valuable tools for precision agriculture and yield-loss mitigation.

**Author Contributions:** Conceptualization, D.T., L.B. and F.S.; methodology, D.T., L.B. and F.S.; formal analysis, D.T., and L.B.; investigation, D.T., L.B., F.A., M.P., R.Q., T.A., H.R., R.E.-V., R.P.Z. and F.S.; data curation, D.T. and L.B.; writing—original draft preparation, D.T. and F.S.; writing—review and editing, D.T., L.B., F.A., M.P., R.Q., T.A., H.R., R.E.-V., R.P.Z. and F.S.; supervision F.S.; project administration, F.S.; funding acquisition, F.S. All authors have read and agreed to the published version of the manuscript.

**Funding:** This research was funded by the French National Centre for Space Studies (CNES) under the QUIMONOS project (Quinoa Monitoring by Satellite). The first author also acknowledges the financial support provided by the Institut de Recherche pour le Développement (IRD).

**Data Availability Statement:** The original contributions presented in this study are included in the article; further inquiries can be directed to the corresponding author.

**Conflicts of Interest:** The authors declare no conflicts of interest.

## References

1. Morita. Chapter 2—Implications of a New Methodology for Assessing Global Water and Food Security Challenges for Agricultural Water Productivity. In *Current Directions in Water Scarcity Research*; Kumar, M.D., Ed.; Water Productivity and Food Security; Elsevier: Amsterdam, The Netherlands, 2021; Volume 3, pp. 11–48.
2. Fuglie, K.O. Is Agricultural Productivity Slowing? *Glob. Food Secur.* **2018**, *17*, 73–83. [CrossRef]

3. Khadatkar, D.R. Optimizing Resource Allocation in Precision Agriculture through the Application of K-Means Clustering. In *Smart Agriculture*; CRC Press: Boca Raton, FL, USA, 2024.
4. Kudoh, K. Considerations on Rice Yield Estimation from the Viewpoints of Crop Science: On a Synthetic Coefficient for the Ddcisive Factors in Yield Estimation. *Jpn. J. Crop Sci.* **1952**, *21*, 7–9. [CrossRef]
5. Tola, D.; Satgé, F.; Pillco Zolá, R.; Sainz, H.; Condori, B.; Miranda, R.; Yujra, E.; Molina-Carpio, J.; Hostache, R.; Espinoza-Villar, R. Soil Salinity Mapping of Plowed Agriculture Lands Combining Radar Sentinel-1 and Optical Sentinel-2 with Topographic Data in Machine Learning Models. *Remote Sens.* **2024**, *16*, 3456. [CrossRef]
6. Tola, D.; Bustillos, L.; Arragan, F.; Chipana, R.; Hostache, R.; Resongles, E.; Espinoza-Villar, R.; Zolá, R.P.; Uscamayta, E.; Perez-Flores, M.; et al. High Spatial Resolution Soil Moisture Mapping over Agricultural Field Integrating SMAP, IMERG, and Sentinel-1 Data in Machine Learning Models. *Remote Sens.* **2025**, *17*, 2129. [CrossRef]
7. Asgari, S.; Hasanlou, M.; Homayouni, S. Enhancing Winter Wheat Yield Estimation Using Machine Learning and Fusion of Radar and Optical Satellite Imagery. *Environ. Sci. Proc.* **2023**, *29*, 65. [CrossRef]
8. Ogungbuyi, M.G.; Mohammed, C.; Fischer, A.M.; Turner, D.; Whitehead, J.; Harrison, M.T. Integration of Drone and Satellite Imagery Improves Agricultural Management Agility. *Remote Sens.* **2024**, *16*, 4688. [CrossRef]
9. Gómez, D.; Salvador, P.; Sanz, J.; Casanova, J.L. Modelling Wheat Yield with Antecedent Information, Satellite and Climate Data Using Machine Learning Methods in Mexico. *Agric. For. Meteorol.* **2021**, *300*, 108317. [CrossRef]
10. Tucker, C.J. Red and Photographic Infrared Linear Combinations for Monitoring Vegetation. *Remote Sens. Environ.* **1979**, *8*, 127–150. [CrossRef]
11. Segarra, J.; González-Torralba, J.; Aranjuelo, Í.; Araus, J.L.; Kefauver, S.C. Estimating Wheat Grain Yield Using Sentinel-2 Imagery and Exploring Topographic Features and Rainfall Effects on Wheat Performance in Navarre, Spain. *Remote Sens.* **2020**, *12*, 2278. [CrossRef]
12. Gómez, D.; Salvador, P.; Sanz, J.; Casanova, J.L. Regional Estimation of Garlic Yield Using Crop, Satellite and Climate Data in Mexico. *Comput. Electron. Agric.* **2021**, *181*, 105943. [CrossRef]
13. Sellers, P.J. Canopy Reflectance, Photosynthesis and Transpiration. *Int. J. Remote Sens.* **1985**, *6*, 1335–1372. [CrossRef]
14. Mutanga, O.; Skidmore, A.K. Narrow Band Vegetation Indices Overcome the Saturation Problem in Biomass Estimation. *Int. J. Remote Sens.* **2004**, *25*, 3999–4014. [CrossRef]
15. Xue, J.; Su, B. Significant Remote Sensing Vegetation Indices: A Review of Developments and Applications. *J. Sens.* **2017**, *2017*, 1353691. [CrossRef]
16. Beck, P.S.A.; Atzberger, C.; Høgda, K.A.; Johansen, B.; Skidmore, A.K. Improved Monitoring of Vegetation Dynamics at Very High Latitudes: A New Method Using MODIS NDVI. *Remote Sens. Environ.* **2006**, *100*, 321–334. [CrossRef]
17. Lobell, D.B.; Thau, D.; Seifert, C.; Engle, E.; Little, B. A Scalable Satellite-Based Crop Yield Mapper. *Remote Sens. Environ.* **2015**, *164*, 324–333. [CrossRef]
18. Hatfield, J.L.; Prueger, J.H.; Sauer, T.J.; Dold, C.; O'Brien, P.; Wacha, K. Applications of Vegetative Indices from Remote Sensing to Agriculture: Past and Future. *Inventions* **2019**, *4*, 71. [CrossRef]
19. Liu, Y.; Fan, Y.; Yue, J.; Ma, Y.; Yang, F.; Fan, J.; Chen, R.; Bian, M.; Feng, H. UAV-Based Remote Sensing Estimation of above-Ground Biomass in Different Crops: A Review. *Int. J. Appl. Earth Obs. Geoinf.* **2025**, *144*, 104938. [CrossRef]
20. Battude, M.; Al Bitar, A.; Morin, D.; Cros, J.; Huc, M.; Marais Sicre, C.; Le Dantec, V.; Demarez, V. Estimating Maize Biomass and Yield over Large Areas Using High Spatial and Temporal Resolution Sentinel-2 like Remote Sensing Data. *Remote Sens. Environ.* **2016**, *184*, 668–681. [CrossRef]
21. Wei, L.; Yang, H.; Niu, Y.; Zhang, Y.; Xu, L.; Chai, X. Wheat Biomass, Yield, and Straw-Grain Ratio Estimation from Multi-Temporal UAV-Based RGB and Multispectral Images. *Biosyst. Eng.* **2023**, *234*, 187–205. [CrossRef]
22. Vahidi, M.; Shafian, S.; Thomas, S.; Maguire, R. Pasture Biomass Estimation Using Ultra-High-Resolution RGB UAVs Images and Deep Learning. *Remote Sens.* **2023**, *15*, 5714. [CrossRef]
23. Biswal, S.; Pathak, N.; Chatterjee, C.; Mailapalli, D.R. Estimation of Aboveground Biomass from Spectral and Textural Characteristics of Paddy Crop Using UAV-Multispectral Images and Machine Learning Techniques. *Geocarto Int.* **2024**, *39*, 2364725. [CrossRef]
24. ten Harkel, J.; Bartholomeus, H.; Kooistra, L. Biomass and Crop Height Estimation of Different Crops Using UAV-Based Lidar. *Remote Sens.* **2019**, *12*, 17. [CrossRef]
25. Luo, S.; Liu, W.; Zhang, Y.; Wang, C.; Xi, X.; Nie, S.; Ma, D.; Lin, Y.; Zhou, G. Maize and Soybean Heights Estimation from Unmanned Aerial Vehicle (UAV) LiDAR Data. *Comput. Electron. Agric.* **2021**, *182*, 106005. [CrossRef]
26. Gao, L.; Chai, G.; Zhang, X. Above-Ground Biomass Estimation of Plantation with Different Tree Species Using Airborne LiDAR and Hyperspectral Data. *Remote Sens.* **2022**, *14*, 2568. [CrossRef]
27. Karim, M.R.; Reza, M.N.; Jin, H.; Haque, M.A.; Lee, K.-H.; Sung, J.; Chung, S.-O. Application of LiDAR Sensors for Crop and Working Environment Recognition in Agriculture: A Review. *Remote Sens.* **2024**, *16*, 4623. [CrossRef]

28. Marcone, A.; Impollonia, G.; Croci, M.; Blandinières, H.; Amaducci, S. Estimation of above Ground Biomass, Biophysical and Quality Parameters of Spinach (*Spinacia oleracea* L.) Using Sentinel-2 to Support the Supply Chain. *Sci. Hortic.* **2024**, *325*, 112641. [CrossRef]
29. Fang, P.; Yan, N.; Wei, P.; Zhao, Y.; Zhang, X. Aboveground Biomass Mapping of Crops Supported by Improved CASA Model and Sentinel-2 Multispectral Imagery. *Remote Sens.* **2021**, *13*, 2755. [CrossRef]
30. Sibanda, M.; Mutanga, O.; Rouget, M. Examining the Potential of Sentinel-2 MSI Spectral Resolution in Quantifying above Ground Biomass across Different Fertilizer Treatments. *ISPRS J. Photogramm. Remote Sens.* **2015**, *110*, 55–65. [CrossRef]
31. Goffart, D.; Curnel, Y.; Planchon, V.; Goffart, J.-P.; Defourny, P. Field-Scale Assessment of Belgian Winter Cover Crops Biomass Based on Sentinel-2 Data. *Eur. J. Agron.* **2021**, *126*, 126278. [CrossRef]
32. Dong, T.; Liu, J.; Qian, B.; He, L.; Liu, J.; Wang, R.; Jing, Q.; Champagne, C.; McNairn, H.; Powers, J.; et al. Estimating Crop Biomass Using Leaf Area Index Derived from Landsat 8 and Sentinel-2 Data. *ISPRS J. Photogramm. Remote Sens.* **2020**, *168*, 236–250. [CrossRef]
33. Veloso, A.; Mermoz, S.; Bouvet, A.; Le Toan, T.; Planells, M.; Dejoux, J.-F.; Ceschia, E. Understanding the Temporal Behavior of Crops Using Sentinel-1 and Sentinel-2-like Data for Agricultural Applications. *Remote Sens. Environ.* **2017**, *199*, 415–426. [CrossRef]
34. Xu, C.; Ding, Y.; Zheng, X.; Wang, Y.; Zhang, R.; Zhang, H.; Dai, Z.; Xie, Q. A Comprehensive Comparison of Machine Learning and Feature Selection Methods for Maize Biomass Estimation Using Sentinel-1 SAR, Sentinel-2 Vegetation Indices, and Biophysical Variables. *Remote Sens.* **2022**, *14*, 4083. [CrossRef]
35. Pilia, S.; Fontanelli, G.; Santurri, L.; Ramat, G.; Baroni, F.; Santi, E.; Lapini, A.; Pettinato, S.; Paloscia, S. Data Integration of Sentinel-1 and Sentinel-2 for Evaluating Vegetation Biomass and Water Status. In Proceedings of the 2023 IEEE International Workshop on Metrology for Agriculture and Forestry (MetroAgriFor), Pisa, Italy, 6–8 November 2023; pp. 694–698.
36. Nuthammachot, N.; Askar, A.; Stratoulias, D.; Wicaksono, P. Combined Use of Sentinel-1 and Sentinel-2 Data for Improving above-Ground Biomass Estimation. *Geocarto Int.* **2022**, *37*, 366–376. [CrossRef]
37. Maxwell, A.E.; Warner, T.A.; Fang, F. Implementation of Machine-Learning Classification in Remote Sensing: An Applied Review. *Int. J. Remote Sens.* **2018**, *39*, 2784–2817. [CrossRef]
38. Belgiu, M.; Drăguţ, L. Random Forest in Remote Sensing: A Review of Applications and Future Directions. *ISPRS J. Photogramm. Remote Sens.* **2016**, *114*, 24–31. [CrossRef]
39. Pelletier, C.; Webb, G.I.; Petitjean, F. Temporal Convolutional Neural Network for the Classification of Satellite Image Time Series. *Remote Sens.* **2019**, *11*, 523. [CrossRef]
40. Satgé, F.; Pillco, R.; Molina-Carpio, J.; Mollinedo, P.P.; Bonnet, M.-P. Reliability of Gridded Temperature Datasets to Monitor Surface Air Temperature Variability over Bolivia. *Int. J. Climatol.* **2023**, *43*, 6191–6206. [CrossRef]
41. Ollivier, C.C.; Carrière, S.D.; Heath, T.; Olioso, A.; Rabefitia, Z.; Rakoto, H.; Oudin, L.; Satgé, F. Ensemble Precipitation Estimates Based on an Assessment of 21 Gridded Precipitation Datasets to Improve Precipitation Estimations across Madagascar. *J. Hydrol. Reg. Stud.* **2023**, *47*, 101400. [CrossRef]
42. Bhargava, A.; Shukla, S.; Ohri, D. Genetic Variability and Interrelationship among Various Morphological and Quality Traits in Quinoa (*Chenopodium quinoa* Willd.). *Field Crops Res.* **2007**, *101*, 104–116. [CrossRef]
43. Satgé, F.; Espinoza, R.; Pillco Zolá, R.; Roig, H.; Timouk, F.; Molina, J.; Garnier, J.; Calmant, S.; Seyler, F.; Bonnet, M.-P. Role of Climate Variability and Human Activity on Poopó Lake Droughts between 1990 and 2015 Assessed Using Remote Sensing Data. *Remote Sens.* **2017**, *9*, 218. [CrossRef]
44. Satgé, F.; Hussain, Y.; Xavier, A.; Zolá, R.P.; Salles, L.; Timouk, F.; Seyler, F.; Garnier, J.; Frappart, F.; Bonnet, M.-P. Unraveling the Impacts of Droughts and Agricultural Intensification on the Altiplano Water Resources. *Agric. For. Meteorol.* **2019**, *279*, 107710. [CrossRef]
45. Perez-Flores, M.; Satgé, F.; Molina-Carpio, J.; Hostache, R.; Pillco-Zolá, R.; Tola, D.; Uscamayta-Ferrano, E.; Bustillos, L.; Bonnet, M.-P.; Duwig, C. Machine-Learning Crop-Type Mapping Sensitivity to Feature Selection and Hyperparameter Tuning. *Remote Sens.* **2026**, *18*, 563. [CrossRef]
46. Stanschewski, C.S.; Rey, E.; Fiene, G.; Craine, E.B.; Wellman, G.; Melino, V.J.; Patiranage, D.S.R.; Johansen, K.; Schmöckel, S.M.; Bertero, D.; et al. Quinoa Phenotyping Methodologies: An International Consensus. *Plants* **2021**, *10*, 1759. [CrossRef] [PubMed]
47. Jiang, J.; Johansen, K.; Stanschewski, C.S.; Wellman, G.; Mousa, M.A.A.; Fiene, G.M.; Asiry, K.A.; Tester, M.; McCabe, M.F. Phenotyping a Diversity Panel of Quinoa Using UAV-Retrieved Leaf Area Index, SPAD-Based Chlorophyll and a Random Forest Approach. *Precis. Agric.* **2022**, *23*, 961–983. [CrossRef]
48. Sesay, S.; Yamaguchi, T.; Kushino, S.; Yoshikawa, Y.; Adachi, S.; Katsura, K. Fusion of UAV-Based 3D Mesh and Spectral Features Improves Quinoa Biomass and LAI Estimation across Genotypic and Temporal Variations. *Smart Agric. Technol.* **2025**, *10*, 100818. [CrossRef]

49. Sesay, S.; Yamaguchi, T.; Kushino, S.; Yoshikawa, Y.; Adachi, S.; Katsura, K. Plant-Level Yield Prediction of Quinoa in Field Plots across Growth Stages Using UAV-Derived 3D Structural and Spectral Features with Machine Learning. *Smart Agric. Technol.* **2026**, *13*, 101940. [CrossRef]
50. Garcia, M.; Raes, D.; Jacobsen, S.-E.; Michel, T. Agroclimatic Constraints for Rainfed Agriculture in the Bolivian Altiplano. *J. Arid Environ.* **2007**, *71*, 109–121. [CrossRef]
51. Canedo, C.; Pillco Zolá, R.; Berndtsson, R. Role of Hydrological Studies for the Development of the TDPS System. *Water* **2016**, *8*, 144. [CrossRef]
52. Bazile, D.; Jacobsen, S.-E.; Verniau, A. The Global Expansion of Quinoa: Trends and Limits. *Front. Plant Sci.* **2016**, *7*, 622. [CrossRef] [PubMed]
53. Jacobsen, S.-E.; Mujica, A.; Jensen, C.R. The Resistance of Quinoa (*Chenopodium quinoa* Willd.) to Adverse Abiotic Factors. *Food Rev. Int.* **2003**, *19*, 99–109. [CrossRef]
54. Bazile, D. Global Trends in the Worldwide Expansion of Quinoa Cultivation. *Biol. Life Sci. Forum* **2023**, *25*, 13. [CrossRef]
55. Risi, J.; Rojas, W.; Pacheco, M. *Producción y Mercado de la Quinua en Bolivia*; Instituto Interamericano de Cooperación para la Agricultura IICA: La Paz, Bolivia, 2015.
56. Agisoft LLC. *Agisoft Metashape Profesional Edition 2016*; Agisoft LLC: St. Petersburg, Russia, 2016.
57. Li, W.; Niu, Z.; Chen, H.; Li, D.; Wu, M.; Zhao, W. Remote Estimation of Canopy Height and Aboveground Biomass of Maize Using High-Resolution Stereo Images from a Low-Cost Unmanned Aerial Vehicle System. *Ecol. Indic.* **2016**, *67*, 637–648. [CrossRef]
58. Laliberte, A.S.; Goforth, M.A.; Steele, C.M.; Rango, A. Multispectral Remote Sensing from Unmanned Aircraft: Image Processing Workflows and Applications for Rangeland Environments. *Remote Sens.* **2011**, *3*, 2529–2551. [CrossRef]
59. Turner, D.; Lucieer, A.; Watson, C. An Automated Technique for Generating Georectified Mosaics from Ultra-High Resolution Unmanned Aerial Vehicle (UAV) Imagery, Based on Structure from Motion (SfM) Point Clouds. *Remote Sens.* **2012**, *4*, 1392–1410. [CrossRef]
60. James, M.R.; Robson, S.; d'Oleire-Oltmanns, S.; Niethammer, U. Optimising UAV Topographic Surveys Processed with Structure-from-Motion: Ground Control Quality, Quantity and Bundle Adjustment. *Geomorphology* **2017**, *280*, 51–66. [CrossRef]
61. North, M.A. A Method for Implementing a Statistically Significant Number of Data Classes in the Jenks Algorithm. In Proceedings of the 6th International Conference on Fuzzy Systems and Knowledge Discovery, Tianjin, China, 14–16 August 2009; Volume 1, pp. 35–38.
62. Sirpa-Poma, J.W.; Satgé, F.; Resongles, E.; Pillco-Zolá, R.; Molina-Carpio, J.; Flores Colque, M.G.; Ormachea, M.; Pacheco Mollinedo, P.; Bonnet, M.-P. Towards the Improvement of Soil Salinity Mapping in a Data-Scarce Context Using Sentinel-2 Images in Machine-Learning Models. *Sensors* **2023**, *23*, 9328. [CrossRef] [PubMed]
63. Gorelick, N.; Hancher, M.; Dixon, M.; Ilyushchenko, S.; Thau, D.; Moore, R. Google Earth Engine: Planetary-Scale Geospatial Analysis for Everyone. *Remote Sens. Environ.* **2017**, *202*, 18–27. [CrossRef]
64. Yu, T.; Zhou, J.; Ranjbar, S.; Chen, J.; Digman, M.F.; Zhang, Z. Evaluation of the Effect of Sentinel-1 SAR and Environmental Factors in Alfalfa Yield and Quality Estimation. *Agronomy* **2024**, *14*, 859. [CrossRef]
65. Breiman, L. Random Forests. *Mach. Learn.* **2001**, *45*, 5–32. [CrossRef]
66. Chen, T.; Guestrin, C. XGBoost: A Scalable Tree Boosting System. In *Proceedings of the 22nd ACM SIGKDD International Conference on Knowledge Discovery and Data Mining*; Association for Computing Machinery: New York, NY, USA, 2016; pp. 785–794.
67. Friedman, J.H. Greedy Function Approximation: A Gradient Boosting Machine. *Ann. Stat.* **2001**, *29*, 1189–1232. [CrossRef]
68. Breiman, L.; Friedman, J.; Olshen, R.A.; Stone, C.J. *Classification and Regression Trees*; Chapman and Hall/CRC: New York, NY, USA, 2017.
69. Wolpert, D.H. Stacked Generalization. *Neural Netw.* **1992**, *5*, 241–259. [CrossRef]
70. Pedregosa, F.; Varoquaux, G.; Gramfort, A.; Michel, V.; Thirion, B.; Grisel, O.; Blondel, M.; Prettenhofer, P.; Weiss, R.; Dubourg, V.; et al. Scikit-Learn: Machine Learning in Python. *J. Mach. Learn. Res.* **2011**, *12*, 2825–2830.
71. LeCun, Y.; Bengio, Y.; Hinton, G. Deep Learning. *Nature* **2015**, *521*, 436–444. [CrossRef] [PubMed]
72. Goodfellow, I.; Bengio, Y.; Courville, A. *Deep Learning*; Adaptive Computation and Machine Learning Series; MIT Press: Cambridge, MA, USA, 2016.
73. Ioffe, S.; Szegedy, C. Batch Normalization: Accelerating Deep Network Training by Reducing Internal Covariate Shift. *arXiv* **2015**. [CrossRef]
74. Srivastava, N.; Hinton, G.; Krizhevsky, A.; Sutskever, I.; Salakhutdinov, R. Dropout: A Simple Way to Prevent Neural Networks from Overfitting. *J. Mach. Learn. Res.* **2014**, *15*, 1929–1958.
75. Kingma, D.P.; Ba, J. Adam: A Method for Stochastic Optimization. *arXiv* **2017**. [CrossRef]
76. Wilson, E.H.; Sader, S.A. Detection of Forest Harvest Type Using Multiple Dates of Landsat TM Imagery. *Remote Sens. Environ.* **2002**, *80*, 385–396. [CrossRef]
77. Huete, A.R.; Liu, H.Q.; Batchily, K.; van Leeuwen, W. A Comparison of Vegetation Indices over a Global Set of TM Images for EOS-MODIS. *Remote Sens. Environ.* **1997**, *59*, 440–451. [CrossRef]

78. Huete, A.R.; Didan, K.; Miura, T.; Rodriguez, E.P.; Gao, X.; Ferreira, L.G. Overview of the Radiometric and Biophysical Performance of the MODIS Vegetation Indices. *Remote Sens. Environ.* **2002**, *83*, 195–213. [CrossRef]
79. Hunt, E.R.; Rock, B.N. Detection of Changes in Leaf Water Content Using Near- and Middle-Infrared Reflectances. *Remote Sens. Environ.* **1989**, *30*, 43–54. [CrossRef]
80. Chen, W.; Liu, L.; Zhang, C.; Wang, J.; Wang, J.; Pan, Y. Monitoring the Seasonal Bare Soil Areas in Beijing Using Multi-Temporal TM Images. In Proceedings of the IGARSS 2004, Anchorage, AK, USA, 20–24 September 2004; Volume 5, pp. 3379–3382.
81. García, M.J.L.; Caselles, V. Mapping Burns and Natural Reforestation Using Thematic Mapper Data. *Geocarto Int.* **1991**, *6*, 31–37. [CrossRef]
82. Key, C.; Benson, N. Landscape Assessment (LA) Sampling and Analysis Methods. In *FIREMON: Fire Effects Monitoring and Inventory System*; U.S. Department of Agriculture, Forest Service, Rocky Mountain Research Station: Fort Collins, CO, USA, 2005; pp. LA 1-51.
83. McFeeters, S.K. The Use of the Normalized Difference Water Index (NDWI) in the Delineation of Open Water Features. *Int. J. Remote Sens.* **1996**, *17*, 1425–1432. [CrossRef]
84. Omuto, C.T.; Vargas, R.R.; El Mobarak, A.M.; Mohamed, N.; Viatkin, K.; Yigini, Y. *Mapeo de Suelos Afectados por Salinidad—Manual Técnico*; FAO: Rome, Italy, 2021.
85. Khan, N.M.; Rastoskuev, V.V.; Sato, Y.; Shiozawa, S. Assessment of Hydrosaline Land Degradation by Using a Simple Approach of Remote Sensing Indicators. *Agric. Water Manag.* **2005**, *77*, 96–109. [CrossRef]
86. Douaoui, A.E.K.; Nicolas, H.; Walter, C. Detecting Salinity Hazards within a Semiarid Context by Means of Combining Soil and Remote-Sensing Data. *Geoderma* **2006**, *134*, 217–230. [CrossRef]
87. Alavipanah, S.K.; Damavandi, A.; Mirzaei, S.; Rezaei, A.; Hamzeh, S.; Matinfar, H.; Teimouri, H.; Javadzarrin, I. Remote Sensing Application in Evaluation of Soil Characteristics in Desert Areas. *Nat. Environ. Change* **2016**, *2*, 1–24. [CrossRef]
88. Dehni, A.; Lounis, M. Remote Sensing Techniques for Salt Affected Soil Mapping: Application to the Oran Region of Algeria. *Procedia Eng.* **2012**, *33*, 188–198. [CrossRef]
89. Khan, N.M.; Rastoskuev, V.V.; Shalina, E.; Sato, Y. Mapping Salt-Affected Soils Using Remote Sensing Indicators-A Simple Approach with the Use of GIS IDRISI. In Proceedings of the 22nd Asian Conference on Remote Sensing (ACRS 2001), Singapore, 5–9 November 2001.
90. Periasamy, S.; Ravi, K.P.; Tansey, K. Identification of Saline Landscapes from an Integrated SVM Approach from a Novel 3-D Classification Schema Using Sentinel-1 Dual-Polarized SAR Data. *Remote Sens. Environ.* **2022**, *279*, 113144. [CrossRef]
91. Attarzadeh, R.; Amini, J.; Notarnicola, C.; Greifeneder, F. Synergetic Use of Sentinel-1 and Sentinel-2 Data for Soil Moisture Mapping at Plot Scale. *Remote Sens.* **2018**, *10*, 1285. [CrossRef]
92. Haralick, R.M.; Shanmugam, K.; Dinstein, I. Textural Features for Image Classification. *IEEE Trans. Syst. Man Cybern.* **1973**, *SMC-3*, 610–621. [CrossRef]
93. Conners, R.W.; Trivedi, M.M.; Harlow, C.A. Segmentation of a High-Resolution Urban Scene Using Texture Operators. *Comput. Vis. Graph. Image Process.* **1984**, *25*, 273–310. [CrossRef]
94. Roberts, D.R.; Bahn, V.; Ciuti, S.; Boyce, M.S.; Elith, J.; Guillera-Arroita, G.; Hauenstein, S.; Lahoz-Monfort, J.J.; Schröder, B.; Thuiller, W.; et al. Cross-Validation Strategies for Data with Temporal, Spatial, Hierarchical, or Phylogenetic Structure. *Ecography* **2017**, *40*, 913–929. [CrossRef]
95. Ploton, P.; Mortier, F.; Réjou-Méchain, M.; Barbier, N.; Picard, N.; Rossi, V.; Dormann, C.; Cornu, G.; Viennois, G.; Bayol, N.; et al. Spatial Validation Reveals Poor Predictive Performance of Large-Scale Ecological Mapping Models. *Nat. Commun.* **2020**, *11*, 4540. [CrossRef] [PubMed]
96. Meyer, H.; Reudenbach, C.; Wöllauer, S.; Nauss, T. Importance of Spatial Predictor Variable Selection in Machine Learning Applications—Moving from Data Reproduction to Spatial Prediction. *Ecol. Model.* **2019**, *411*, 108815. [CrossRef]
97. Hu, W.; Huang, Y.; Wei, L.; Zhang, F.; Li, H. Deep Convolutional Neural Networks for Hyperspectral Image Classification. *J. Sens.* **2015**, *2015*, 258619. [CrossRef]
98. Guan, H.; Yu, Y.; Ji, Z.; Li, J.; Zhang, Q. Deep Learning-Based Tree Classification Using Mobile LiDAR Data. *Remote Sens. Lett.* **2015**, *6*, 864–873. [CrossRef]
99. Wallace, L.; Lucieer, A.; Watson, C.; Turner, D. Development of a UAV-LiDAR System with Application to Forest Inventory. *Remote Sens.* **2012**, *4*, 1519–1543. [CrossRef]
100. Hütt, C.; Bolten, A.; Hüging, H.; Bareth, G. UAV LiDAR Metrics for Monitoring Crop Height, Biomass and Nitrogen Uptake: A Case Study on a Winter Wheat Field Trial. *PFG J. Photogramm. Remote Sens. Geoinf. Sci.* **2023**, *91*, 65–76. [CrossRef]
101. Huang, R.; Yao, W.; Xu, Z.; Cao, L.; Shen, X. Information Fusion Approach for Biomass Estimation in a Plateau Mountainous Forest Using a Synergistic System Comprising UAS-Based Digital Camera and LiDAR. *arXiv* **2022**. [CrossRef]
102. Aasen, H.; Burkart, A.; Bolten, A.; Bareth, G. Generating 3D Hyperspectral Information with Lightweight UAV Snapshot Cameras for Vegetation Monitoring: From Camera Calibration to Quality Assurance. *ISPRS J. Photogramm. Remote Sens.* **2015**, *108*, 245–259. [CrossRef]

103. Hunt, R.; Hively, W.D.; Fujikawa, S.J.; Linden, D.S.; Daughtry, C.S.T.; McCarty, G.W. Acquisition of NIR-Green-Blue Digital Photographs from Unmanned Aircraft for Crop Monitoring. *Remote Sens.* **2010**, *2*, 290–305. [CrossRef]
104. Bendig, J.; Bolten, A.; Bennertz, S.; Broscheit, J.; Eichfuss, S.; Bareth, G. Estimating Biomass of Barley Using Crop Surface Models (CSMs) Derived from UAV-Based RGB Imaging. *Remote Sens.* **2014**, *6*, 10395–10412. [CrossRef]
105. Bendig, J.; Yu, K.; Aasen, H.; Bolten, A.; Bennertz, S.; Broscheit, J.; Gnyp, M.L.; Bareth, G. Combining UAV-Based Plant Height from Crop Surface Models, Visible, and near Infrared Vegetation Indices for Biomass Monitoring in Barley. *Int. J. Appl. Earth Obs. Geoinf.* **2015**, *39*, 79–87. [CrossRef]
106. Han, L.; Yang, G.; Dai, H.; Xu, B.; Yang, H.; Feng, H.; Li, Z.; Yang, X. Modeling Maize Above-Ground Biomass Based on Machine Learning Approaches Using UAV Remote-Sensing Data. *Plant Methods* **2019**, *15*, 10. [CrossRef] [PubMed]
107. Myneni, R.B.; Ramakrishna, R.; Nemani, R.; Running, S.W. Estimation of Global Leaf Area Index and Absorbed Par Using Radiative Transfer Models. *IEEE Trans. Geosci. Remote Sens.* **1997**, *35*, 1380–1393. [CrossRef]
108. Geng, L.; Che, T.; Ma, M.; Tan, J.; Wang, H. Corn Biomass Estimation by Integrating Remote Sensing and Long-Term Observation Data Based on Machine Learning Techniques. *Remote Sens.* **2021**, *13*, 2352. [CrossRef]
109. Zhang, P.; Lu, B.; Ge, J.; Wang, X.; Yang, Y.; Shang, J.; La, Z.; Zang, H.; Zeng, Z. Using UAV-Based Multispectral and RGB Imagery to Monitor above-Ground Biomass of Oat-Based Diversified Cropping. *Eur. J. Agron.* **2025**, *162*, 127422. [CrossRef]
110. Maimaitijiang, M.; Sagan, V.; Sidike, P.; Daloye, A.M.; Erkbol, H.; Fritschi, F.B. Crop Monitoring Using Satellite/UAV Data Fusion and Machine Learning. *Remote Sens.* **2020**, *12*, 1357. [CrossRef]
111. Frampton, W.J.; Dash, J.; Watmough, G.; Milton, E.J. Evaluating the Capabilities of Sentinel-2 for Quantitative Estimation of Biophysical Variables in Vegetation. *ISPRS J. Photogramm. Remote Sens.* **2013**, *82*, 83–92. [CrossRef]
112. Kumar, S.; Ghosh, S.S.; Mandal, D.; Bhattacharya, A.; Porwal, A.; Karthikeyan, L. Enhancing Vegetation Monitoring: A Proposal for a Sentinel-2 Based Vegetation Health Index. *Front. Remote Sens.* **2025**, *6*, 1581355. [CrossRef]
113. Villarroya-Carpio, A.; Lopez-Sanchez, J.M.; Engdahl, M.E. Sentinel-1 Interferometric Coherence as a Vegetation Index for Agriculture. *Remote Sens. Environ.* **2022**, *280*, 113208. [CrossRef]
114. Khabbazan, S.; Vermunt, P.; Steele-Dunne, S.; Ratering Arntz, L.; Marinetti, C.; van der Valk, D.; Iannini, L.; Molijn, R.; Westerdijk, K.; van der Sande, C. Crop Monitoring Using Sentinel-1 Data: A Case Study from The Netherlands. *Remote Sens.* **2019**, *11*, 1887. [CrossRef]
115. Bao, X.; Zhang, R.; Lv, J.; Wu, R.; Zhang, H.; Chen, J.; Zhang, B.; Ouyang, X.; Liu, G. Vegetation Descriptors from Sentinel-1 SAR Data for Crop Growth Monitoring. *ISPRS J. Photogramm. Remote Sens.* **2023**, *203*, 86–114. [CrossRef]
116. Nduku, L.; Munghemezulu, C.; Mashaba-Munghemezulu, Z.; Ratshiedana, P.E.; Sibanda, S.; Chirima, J.G. Synergetic Use of Sentinel-1 and Sentinel-2 Data for Wheat-Crop Height Monitoring Using Machine Learning. *AgriEngineering* **2024**, *6*, 1093–1116. [CrossRef]
117. Mercier, A.; Betbeder, J.; Rapinel, S.; Jegou, N.; Baudry, J.; Hubert-Moy, L. Evaluation of Sentinel-1 and -2 Time Series for Estimating LAI and Biomass of Wheat and Rapeseed Crop Types. *J. Appl. Remote Sens.* **2020**, *14*, 024512. [CrossRef]
118. Jiao, X.; McNairn, H.; Yekkehkhany, B.; Dingle Robertson, L.; Ihuoma, S. Integrating Sentinel-1 SAR and Sentinel-2 Optical Imagery with a Crop Structure Dynamics Model to Track Crop Condition. *Int. J. Remote Sens.* **2022**, *43*, 6509–6537. [CrossRef]
119. Gitelson, A.A. Wide Dynamic Range Vegetation Index for Remote Quantification of Biophysical Characteristics of Vegetation. *J. Plant Physiol.* **2004**, *161*, 165–173. [CrossRef] [PubMed]
120. Flores, L.; Nendel, C.; Bookhagen, B.; Oviedo Reyes, J.A.; Smith, T.; Ghazaryan, G. The Potential of Sentinel-1 Time Series for Large-Scale Assessment of Maize and Wheat Phenology across Germany. *GISci. Remote Sens.* **2025**, *62*, 2531593. [CrossRef]
121. Hastie, T.; Tibshirani, R.; Friedman, J. *The Elements of Statistical Learning: Data Mining, Inference, and Prediction*, 2nd ed.; Springer Series in Statistics; Springer Science & Business Media: New York, NY, USA, 2009.
122. Guyon, I.; Elisseeff, A. An Introduction of Variable and Feature Selection. *J. Mach. Learn. Res. Spec. Issue Var. Feature Sel.* **2003**, *3*, 1157–1182. [CrossRef]
123. Kiranyaz, S.; Avci, O.; Abdeljaber, O.; Ince, T.; Gabbouj, M.; Inman, D.J. 1D Convolutional Neural Networks and Applications: A Survey. *Mech. Syst. Signal Process.* **2021**, *151*, 107398. [CrossRef]
124. Dietterich, T.G. Ensemble Methods in Machine Learning. In *Proceedings of the Multiple Classifier Systems*; Springer: Berlin/Heidelberg, Germany, 2000; pp. 1–15.
125. Holman, F.H.; Riche, A.B.; Michalski, A.; Castle, M.; Wooster, M.J.; Hawkesford, M.J. High Throughput Field Phenotyping of Wheat Plant Height and Growth Rate in Field Plot Trials Using UAV Based Remote Sensing. *Remote Sens.* **2016**, *8*, 1031. [CrossRef]
126. Wang, T.; Liu, Y.; Wang, M.; Fan, Q.; Tian, H.; Qiao, X.; Li, Y. Applications of UAS in Crop Biomass Monitoring: A Review. *Front. Plant Sci.* **2021**, *12*, 616689. [CrossRef] [PubMed]




https://doi.org/10.3390/rs18173017